K.K. Kirov, Yu. Baranov, J. Mailloux, M.-L. Mayoral, M.F.F. Nave, J. Ongena
and JET EFDA contributors

LH Power Deposition and CD Efficiency Studies by Application of Modulated Power at JET

LH Power Deposition and CD Efficiency Studies by Application of Modulated Power at JET

K.K. Kirov[1], Yu. Baranov[1], J. Mailloux[1], M.-L. Mayoral[1], M. F. F. Nave[2],
J. Ongena[3] and JET EFDA contributors*

JET-EFDA, Culham Science Centre, OX14 3DB, Abingdon, UK

[1]*EURATOM-CCFE Fusion Association, Culham Science Centre, OX14 3DB, Abingdon, OXON, UK*
[2] *Associação EURATOM/IST, Instituto de Plasmas e Fusão Nuclear, Lisbon, Portugal*
[3] *Plasmaphysics Lab, ERM-KMS, Association EURATOM-Belgian State, Brussels, Belgium. TEC partner*
* See annex of F. Romanelli et al, "Overview of JET Results",
(Proc. 22 [nd] IAEA Fusion Energy Conference, Geneva, Switzerland (2008)).

ABSTRACT.

The LH power deposition and the CD efficiency were assessed by application of modulated LH power. Density and magnetic field scans were performed and the response of the electron temperature provided by the available ECE diagnostic was investigated by means of FFT analysis. An innovative technique based on comparison between modelled and experimental data was developed and used in the study. The LH waves are absorbed by fast electrons with energies of a few times the thermal one, causing a modification in the Electron Distribution Function (EDF) by creating a plateau in parallel direction. The phase of the temperature perturbations, ϕ, as well as the ratio between the amplitudes of the third and the main harmonics, $\delta T_{e3}/\delta T_{e1}$, are found to be strongly affected by the plateau of the EDF as the broader the plateau the larger $|\phi|$, ($\phi<0$), and the smaller $\delta T_{e3}/\delta T_{e1}$ are. Transport and Fokker-Planck modelling was used to support this conclusion and to interpret the experimental data hence to assess the LH CD efficiency and deposition profile. The results from the analysis are consistent with broad off-axis LH power deposition profile. For densities between $1\times10^{19}\mathrm{m}^{-3}$ and $4\times10^{19}\mathrm{m}^{-3}$, which is the accessibility limit at the highest magnetic field discharges a gradual shift of the maximum of the power deposition to the periphery and a degradation of the CD efficiency was observed.

1. INTRODUCTION

The Lower Hybrid Current Drive (LHCD) system at JET uses Radio Frequency (RF) waves in the Lower Hybrid (LH) range of frequencies to heat the plasma and generate a toroidal electric current. LHCD is widely recognised as the most efficient non-inductive current source [1] as it features the highest current drive (CD) per unit of coupled RF power.

Substantial theoretical work [1-3] on the LH waves coupling, propagation and absorption has been carried out from the early 70s until late 90s. Progress in understanding the physics of RF heated plasmas later encouraged the implementation of LHCD systems on many tokamaks, including JET, JT60-U, Tore Supra, Alcator C-mod, ASDEX, etc. In parallel, a considerable amount of codes based on the linear theory and calculating the LH wave absorption and the driven current were developed and used to model and to predict the experimental data. Most of the existing numerical tools [4-10] are based on a combination of Ray Tracing (RT) and Fokker Planck (FP) codes. Full wave code [11] has been recently reported as well.

The experimental verification of the LH power deposition and CD efficiency is essential for better understanding of the processes involved in the wave propagation and absorption. Studies on this subject are important because of their capability to provide a benchmark against the existing codes. In addition fundamental issues related to the possible use of LHCD systems in the next-generation fusion devices as for example ITER can be clarified and better understood. Moreover crucial parameters regarding the implementation of the LHCD system in ITER were proposed mainly by means of numerical simulations [12, 13], which further highlights the necessity of experimental validation. A recent review on the possible ITER steady-state scenarios [13] requested more comparison between measured and predicted LH current density profiles.

Recent experimental research focusses on LH wave propagation and CD studies at low density, whilst the high-density regime remains mainly unexplored. Early experimental studies [14,15] reported an unpredicted decrease of the CD effects with increase of the plasma density. Several attempts to assess the LH power deposition and CD efficiency from the available experimental data have been reported [4, 14, 16]. The results in [4, 16] are in qualitative agreement with theoretical predictions at low plasma density. All these studies include indirect methods as they use supplementary information provided by diagnostics related to the fast electrons generated by the applied LH power. For instance in [4, 16], hard X-ray diagnostic measuring the bremsstrahlung radiation by electrons with energies between 80keV and 300keV was used to detect the fast electrons. The novelty in the study presented here is in the use of LH power modulation and FFT analysis of the induced changes on the electron temperature profile measured by Electron Cyclotron Emission (ECE) to assess the LH wave absorption and CD efficiency. This is also an indirect method but its advantage is that it provides both, the deposition profile and the CD efficiency, by means of standard ECE measurements, which are implemented on most of the present tokamaks.

Modulated power is a well-known tool to diagnose the Electron Cyclotron Resonance Heating (ECRH) power deposition profile [17] and Ion Cyclotron Resonance Heating — Mode Conversion (ICRH-MC) absorbed power [18]. A straightforward application of this technique to the LH case, however, is not trivial. The reason is that LH does not heat directly the thermal electrons, which are diagnosed by standard ECE measurements. Consequently, the changes of the electron temperature do not follow exactly the LH power input. It is well known [1] that the wave energy is dissipated collisionlessly on fast electrons via Landau damping. The resonant electrons have velocities that are usually at least a few times larger than the thermal velocity and therefore they transfer their energy to the bulk electrons not immediately but on a time scale much longer than the thermal collisional time. In addition, the radial transport of the fast electrons has to be considered; however, it has been shown [19] that for typical JET conditions the collisional slowing down of the fast electrons prevails on the radial diffusion.

The deposition profile detection is also affected by the heat transport, as the heat wave will propagate outside the region where the LH wave is absorbed. The broadening of the electron temperature perturbations vanishes if the heating power is modulated at infinitely high frequency [17]. The modulation frequency is, however, limited by the sensitivity of the measurements of the temperature perturbations. There is an additional limitation, which is related to the time delay between the absorption of the LH power by the fast electrons and collisional transfer of the power to the bulk electrons as discussed in detail in this paper. Although high frequency modulation is beneficial regarding the suppression of the transport effects one clear disadvantage is that on a short time scale, associated with the high frequency, the energy transferred to the thermal electrons becomes smaller and undetectable. Therefore the range of modulation frequencies should be carefully selected.

Supra-thermal electrons produced by the LH power can pollute the ECE measurements. The fast electrons may affect the measured electron temperature due to the large relativistic downshift of

their third harmonic emission to the second harmonic frequency. Special attention has been paid to this effect when interpreting the experimental results. In plasmas with medium and large densities it was found that the impact of the fast electrons on the ECE measurements is negligible.

The processes related to the LH wave damping and heat wave propagation are discussed in detail in this paper. Their contribution is taken into account when interpreting the experimental and numerical data. The LH power deposition profile and the CD efficiency are assessed after implementing transport and FP modelling [20, 21]. The paper is organised as follows. Section 2 explains the experimental setup and the diagnostics used. A short description of the main theoretical relations and the transport modelling is given in Section 3. Section 4 discusses the most important experimental results, while the Section 5 summarises the observations.

2. EXPERIMENTAL SETUP AND DIAGNOSTICS

2.1. LHCD SYSTEM AT JET

The LHCD system at JET is described in detail in [22, 23]. It operates at a frequency $f_{LH} = \omega_{LH}/2\pi$ = 3.7GHz. The power spectrum of the launched LH wave as a function of the parallel refractive index $N_{\parallel}$ can be changed by varying the phase shift between the klystrons. In the experiments presented here they were pulsed in phase so that the spectrum was peaked at $N_{\parallel} = 1.84$.

The LH power waveform in JET is controlled by dedicated software, the so-called local manager, which runs the whole plant during the pulse. In order to allow modulation at frequencies higher than 10Hz an upgrade of the local manager was done. Due to technical requirements there were a limited number of available modulation frequencies f: 20.83Hz, 31.25Hz, 41.67Hz and 62.5Hz. Most of the experiments were done at 41.67Hz, as explained below. This frequency was found to be most suitable for the measurements of the CD efficiency. A square modulation waveform was used in all the experiments, which allowed investigating the main and higher harmonics of f. We use the ratio $(P_{LH,max}-P_{LH,min})/(P_{LH,max}+P_{LH,min})$ as modulation depth, where $P_{LH,max}$ and $P_{LH,min}$ are the maximum and minimum of the coupled LH power. Most of the investigated cases use waveforms with maximum and minimum amplitude of about 3MW and 0.5MW, respectively, in which cases the modulation depth was about 71%. In reality the launched LH power was slightly different from the ideal square waveform. This resulted in a deviation of the normalised amplitude of the 1st harmonic of f from $4/\pi$ (≈ 1.27) in the ideal case to about 1.23. The ratio of the 3rd to the 1st harmonic in the LH power waveform is estimated to be about 0.30, i.e. 10% lower than the corresponding ratio for ideal rectangular waveform ($1/3 \approx 0.33$).

2.2. ECE AND ESSENTIAL DIAGNOSTICS

The ECE heterodyne radiometer at JET [24] consists of 96 channels which were used in 2nd harmonic X-mode. At the magnetic configurations of interest they cover almost the whole plasma cross section, except the very core and the very inner part of the high field side of the torus. These regions were excluded from the analysis. The data were collected with a sampling frequency of either 1kHz or

5kHz. The radial position is determined by mapping on the outboard midplane using the magnetic equilibrium calculated by EFIT. The radial resolution ranges from 0.02m to 0.05m, whilst the accuracy of electron temperature data from ECE is assessed to be around 10%.

The electron density is obtained by means of the Thomson Scattering (TS) measurements based on the LIght Detection And Ranging (LIDAR) technique [25]. This diagnostic also provides the electron temperature and is used to check the reliability of the ECE data. The diagnostic is capable to provide one profile every 0.25s with a spatial resolution of about 0.12m. In some cases the resolution and the accuracy of LIDAR TS are not satisfactory and therefore, whenever possible the High Resolution Thomson Scattering (HRTS) diagnostic was used to measure the electron density and temperature. The error bars on the density profiles provided by the HRTS diagnostic are assessed to be between 5% and 10%. During pulses with Neutral Beam (NB) power the Charge Exchange (CX) diagnostic was used to deduce the ion temperature profiles, T_i, needed in the transport simulations. As for the ECE diagnostic, all the data and modelling results are mapped on the outboard midplane and the corresponding profiles are given versus the midplane radius R.

An example of a discharge with LH modulation at 41.67Hz is shown in figure 1a. The electron temperature modulations are clearly visible, well above the noise level, which is below 10eV at 41.67Hz and 1eV for 125Hz. The amplitudes, $\delta T_{e1,3}$, of the 1st and 3rd harmonic and the phase, ϕ, of the Fast Fourier Transform (FFT) of T_e perturbations are shown in figure 1b. The phase of the temperature perturbations is in fact the difference between the first harmonic phases of the electron temperature and the LH power perturbations. It is always negative which is in agreement with the causality principle and reflects the fact that electron temperature changes are caused by the heating power perturbations.

2.3 EFFECT OF NON THERMAL EMISSION ON THE ECE MEASUREMENTS

LH waves can influence the ECE measurements. Depending on the electron density some of the ECE channels near the edge, where the optical thickness is small, can be affected by the down shifted non-thermal emission by the fast electrons. As a result of this a peculiar high-temperature tail forms in a narrow region near the edge. Consistency checks with TS data were done and the channels, which are affected by the fast electrons, mainly channels near the edge, were dropped and not used in the study. In addition to this the optical thickness of the plasma in the region of interest was assessed and discussed in [26]. It was found that in the investigated experiments the optical thickness was sufficiently high over a broad region in the plasma excluding the peripheral part near the edge.

Electron temperature measurements based on ECE emission are valid, in general, in optically thick Maxwellian plasmas. The Electron Distribution Function (EDF) may strongly deviate from Maxwellian in the presence of LH power, which typically affects the high-energy tail of EDF where the electron velocities, v, are much larger than the thermal velocity $v_{te} = (T_e/m_e)^{1/2}$. Figure 2 shows schematically different regions where electrons can produce emission at a given frequency $\omega_{obs} = 2\omega_{ce}(R_{obs}) = 2q_e B(R_{obs})/m_e$, where q_e is the electron charge, m_e is the electron rest mass, ω_{ce}

4

is the electron cyclotron frequency and $B(R_{obs})$ is the magnetic field at the observation radius R_{obs}. Only emission in the equatorial plane perpendicular to the magnetic field is considered here since the ECE antenna pattern is relatively narrow so that the Doppler shift effects can be neglected [16]. In a Maxwellian plasma with temperature of a few keV the non-thermal downshifted emission is small and can be neglected. In the presence of the high-energy tail, however, the non-thermal contribution may become significant. In the optically thick plasma the downshifted 2nd and 3rd harmonic emission produced in the region $R<R_{obs}$ is reabsorbed by the thermal electrons in the vicinity of the resonance layer, where $\omega_{obs} = 2\omega_{ce}$ and therefore does not affect the measurements. Emission produced in the region $R>R_{obs}$ at the 3rd harmonic downshifted to ω_{obs} is received by the antenna, which is shown schematically at the separatrix location in figure 2. The measurements are taken close to the equatorial plane beyond the plasma boundary in the region of low magnetic field.

The 3rd harmonic emission of the fast electrons with kinetic energy E_e and located at $R>R_{obs}$ can be detected at a given frequency ω_{obs} if the following condition is fulfilled:

$$\omega_{obs} = 2\omega_{ce}\,(R_{obs}) = 2q_e B(R_{obs})/m_e = 3\omega_{ce}\,(R)/\gamma \tag{1}$$

where $\gamma = (1-v^2/c^2)^{-1/2}$ is the relativistic factor. Fast electrons with energies of about 100keV and higher can be produced by either the toroidal electric field E or by the LH waves. In the experiment discussed in this paper, a typical normalised electric field is assessed to be $E/E_{dr}<0.003$, where $E_{dr}= m_e v_{te}/q_e \tau_{te}$ and τ_{te} is the electron collisional time. An electric field at such low level does not produce a significant amount of electrons with energy of 100keV and above, as it has been verified by a solution of the relativistic FP equation discussed below.

The LH wave accelerates fast electrons if its phase velocity along the magnetic field line is equal to the parallel velocity of the resonant electrons leading to the resonant condition, which relates the parallel velocity of the resonant fast electrons to the parallel refractive index, $N_\|$, of the LH wave:

$$v_{ph} = \omega_{LH}/k_{//} = c/N_{//} = v_{//} \tag{2}$$

Here v_{ph} is the phase velocity of the LH wave, whilst $k_\|$ and $v_\|$ are the components of the wave vector and electron velocity along the magnetic field line. The perpendicular velocity of the fast electrons is much smaller than the parallel, i.e. $v \approx v_\| = c/N_\|$. Using this approximation we can deduce the relation between the electron energy E_e and $N_\|$ as well as the phase curves $(N_\|, R)$ and (E_e, R) for electrons emitting at given frequency ω_{obs}.

In figure 3a four example curves, numbered 1 to 4, are given for four different frequencies ω_{obs}. The observation points, R_{obs}, are shown by $+$ sign, while the corresponding frequency ω_{obs} can be found from figure 2. The energy required by fast electrons at given position to emit their downshifted 3rd harmonic at ω_{obs} can be derived directly from equation (1). In figure 3b the phase curves in (E_e, R) space corresponding to the same frequencies as in figure 3a are given and also numbered 1 to 4. In

these examples the separatrix is located at $R = 3.86$m, while acceleration of fast electrons beyond this radius is assumed to be negligible. Further the range of $N_{\parallel}$ allowed in the plasma is examined in order to assess the corresponding energy of the resonant electrons. The accessibility condition [27, 28]:

$$N_{\parallel acc} = \omega_{pe}/\omega_{ce} + (1 + (\omega_{pe}/\omega_{ce})^2 - \sum_i (\omega_{pi}/\omega_{LH})^2)^{1/2} \qquad (3)$$

is used in order to estimate the minimum $N_{\parallel}$ of the LH wave. Only $N_{\parallel} > N_{\parallel \, acc}$ is allowed at certain position in the plasma and the corresponding $N_{\parallel \, acc}$ is determined by (3) and related to the plasma density and the magnetic field via ω_{ce} and the electron and ion plasma, $\omega_{pe,i}$, frequencies.

The minimum $N_{\parallel}$ allowed in the plasma is plotted in figure 3a for two pulses at 3.4T low (L-line) and high (H-line) density. The region located below the L- and H-lines has to be excluded from the analysis. Accordingly the parts of the ($N_{\parallel}$, R) phase curves above L- and H-lines indicate in each case the space, where interaction between fast electrons emitting at ω_{obs} and LH wave is allowed by the accessibility condition. Making use of the relation between $N_{\parallel}$ and E_e and equation (3) the L- and H-lines are plotted in (E_e, R) space, figure 3b, to show the upper limit of the energy of the fast electrons accelerated by the LH waves. Again no electrons emitting at ω_{obs} and with energy above L- and H-lines are created by LH waves as constrained by the accessibility condition (3).

Analysing the intersection of the (E_e, R) phase curves with the accessibility lines, i.e. the L- and H-lines in figure 3b, one can conclude that the maximum energy of the fast electrons emitting at ω_{obs} increases when plasma density decreases. Also the region where non-thermal emission is allowed extends towards the plasma core at lower density and higher magnetic field as the accessibility condition allows LH wave propagation with wider range of $N_{\parallel}$. In addition, one can make the following observation: the closer the observation point to the magnetic axis the longer the phase curve available for the fast electrons emitting at the observation frequency ω_{obs}. Indeed, for the observation point 1 in figure 3a and 3b the acceleration is allowed in the range of energies 105keV<E_e<144keV in the case of low density and 105keV<E_e<123keV in the case of high density plasma. For the observation point 4 the acceleration is allowed only in the case of low density plasma in the range 225keV<E_e<235keV.

A particular case for $R_{obs} = 3.3$m is analysed by following curve 2 from the + point towards the edge, figure 3a and 3b. In the low density case, L-line, it can be concluded that in order to affect T_e measurements at R_{obs} there should be significant amount of fast electrons in the region 3.72m<R<3.86m with kinetic energy between 144keV and 170keV. This condition corresponds to interaction with LH waves with parallel refractive index in the range 1.52<$N_{\parallel}$<1.6. As noted in the previous section the launched $N_{\parallel}$ spectrum by the LH antenna has its peak at $N_{\parallel,max} = 1.84$, while the fraction of the LH power launched at $|N_{\parallel}|$<1.6 is assessed less than 4%. The LH power for 1.5<$N_{\parallel}$<1.6 is even smaller and that means negligible number of fast electrons with energies in the range 144keV<E_e<170keV, figure 3b, are produced by the LH wave so that it has relatively small impact on the ECE measured T_e at $R_{obs} = 3.3$m.

6

More comprehensive assessment of the impact of the LH waves on the ECE measurements would require finding the anti-Hermitian part of the dielectric tensor. Although, such an analysis is out of the scope of this paper, an approximate estimate of the impact of the fast electrons of ECE measurements was done for a particular case of the low density JET Pulse No: 73473. ECE emission was derived according to the procedure given in [29]. It was found that the ECE measurement at $R = 3.54$m will be only slightly affected by the fast electrons at $R > 3.54$m; the real electron temperature, $T_e \approx 1$keV, in this case was found to be about 1% lower than what the ECE diagnostic will detect. For measurements at larger R the impact of the fast electrons is expected even smaller as the width of the resonant region decreases, figure 3b. These arguments create a basis for further analysis of the T_e profile from ECE measurements in the presence of LH waves.

2.4 FFT ANALYSIS OF THE DATA

The study is based on the FFT of the ECE data so details of the procedure used, estimates of the errors and their sources is given here. The time slices of the data were selected to be multiples of the periods of the modulation so that the spectral leakage will be minimal [30]. The latter is possible as the modulation frequency is known. For instance in the case of 41.67Hz modulations FFT time interval of 0.96s is found the best compromise between accuracy and stable plasma conditions.

The errors in the amplitude of T_e perturbations were assessed by means of spectrograms. This method utilises Short Time Fourier Transform (STFT), e.g. in figure 1a STFTs are performed over 38 time windows with a width of 0.512s and a time shift between them of 0.012s. The first window is centred at 25.756s while the last one at 26.204s. The resultant 38 FFT spectra are then analysed statistically and the standard deviation of the amplitude is taken as an estimate of the δT_e error bars. In addition to that the noise levels were estimated by averaging over the amplitudes of the temperature perturbations at two frequencies adjacent to f.

Large variations of δT_e are found mainly for the central ECE channels, $R < 3.2$-3.4m, figure 1b. In this case the amplitude was found significantly affected by the sawteeth. Although their frequency, ≈ 10Hz, is lower than the modulation used, the wide frequency spectrum associated with a sudden sawtooth crash impacts on the amplitude and the phase of the perturbation on the modulation frequency.

The highest density cases were in general noisier. ELMs were found to affect the measurements significantly. Although their frequency was again different from the one used in the modulations it was found that the whole spectrum of the measured ECE data, especially channels near the edge, was distorted by the ELMs. MHD events also affect the phase but to a smaller extent.

3. THEORETICAL BACKGROUND AND INTEGRATED MODELLING

Essential issues related to the power absorption and the heat wave transport will be discussed first in order to highlight the fundamental dependencies and relations. A brief account of the processes involved in the T_e evolution will be given in the next section.

3.1. BASIC PHYSICS RELATIONS

As this study relies on T_e measurements, the electron energy balance equation is of main interest here. Its most general form reads:

$$\frac{3}{2}\frac{\partial n_e T_e}{\partial t} = -\nabla q_e + p_B + p_C; \quad q_e = -n_e \chi_e \nabla q_e; \tag{4}$$

It will be further assumed that the application of LH power changes T_e only and its impact on all other quantities in (4) is through T_e. No changes of plasma density, n_e, with the application of LH power are assumed as well. All contributions to the power inputs and sinks are accounted for in p_B; it includes Ohmic and non-LH auxiliary heating, power lost by radiation and electron-ion energy exchange. The heat flux q_e is assumed purely diffusive, whilst the power density p_C accounts for the RF heating power of interest. As the auxiliary heating is by application of LH power two notations are used to distinguish between the collisional power, which heats thermal electrons, p_C, and the absorbed LH power, p_W. In steady state p_C and p_W are equal as all the absorbed wave power is transferred via collisions to the bulk electrons; however, when transient events are investigated p_C and p_W evolve on a different time scale. When axial-symmetric configurations are considered (4) can be presented on a one dimensional transport mesh or co-ordinate system consisting of the normalised radius ρ only. Equation (4) also describes the excitation and propagation of temperature perturbations when the source p_C is modulated with frequency $f=\omega/2\pi$.

All perturbed quantities are characterised by their amplitude (indicated with a tilde sign on top) and an oscillating part, $e^{-i\omega t}$. The amplitude can be presented by its magnitude, denoted by prefix δ, sometimes also called amplitude, and phase: ϕ for T_e and φ for p_C. For example the expressions for T_e and p_C perturbations are as follows:, $T_e = \tilde{T}_e e^{-i\omega t}$, $\tilde{T}_e = \delta T_e e^{-i\phi}$, $p_c = \tilde{p}_c e^{-i\omega t}$, $\tilde{p}_c = \delta p_c e^{-i\varphi}$. Equation (4) then transforms into:

$$\frac{3}{2} i\omega n_e \tilde{T}_e = -\nabla \tilde{q}_e + \tilde{p}_B + \tilde{p}_C \tag{5}$$

A sketch of the power deposition profile, p_C, in figure 4a illustrates the basic geometrical definitions in the study. The deposition free region will be referred to as the region where the absorbed LH power is absent or negligible compared to the other contributions in the power balance. The deposition will be characterised by its location, blue area in figure 4a, and maximum, which will be also referred to as a deposition centre. The simplified temperature profile in figure 4a aims to show the different regions with respect to the transport: the core, the stiff region and the edge.

The electron heat transport is determined by turbulence [31] over a broad region in the plasma core. Finding the exact form of the heat flux and its dependence on plasma parameters is a subject of many dedicated studies [32]. In general one can use first principle models, e.g. transport based on the ITG turbulence, or more general empirical model which retains the main feature of the turbulent transport, i.e. the heat flux increases significantly when the ratio of $\nabla T_e/T_e$ exceeds a

critical value $(\nabla T_e/T_e)|_{cr}$. The region where this is applicable, between the very core and the edge, is noted as stiff region in figure 4a.

Figure 4b shows the relation between different codes and diagnostics involved in the integrated modelling and data analysis. When LH wave is launched into the plasma, its power decreases as the resonant fast electrons absorb energy from the wave. As a result of this EDF is modified and a non-inductive current with density j_W is driven. The dissipated wave power p_W is, however, different from the power p_C absorbed by the bulk electrons with velocities smaller or comparable to the thermal one. The energy exchange time between the fast and thermal electrons is determined by collisions between the two species and is usually much larger than the collision time between bulk electrons. As a result p_C is expected to increase slowly after the switch on of LH power. In a longer time scale p_C and p_W will equalise, meaning that for cw applications the knowledge of one of them is sufficient. In contrast when studying transient events, using modulation or by switching on/off the LH power, p_C and p_W waveforms will be different which becomes more pronounced at higher frequencies or shorter time scales.

The electron temperature evolution in the presence of the modulated LH power was studied by means of the transport code JETTO [33]. The code provides a set of transport models to choose from and also allows implementation of new models. In JETTO the absorbed LH power is treated as direct electron heat source, i.e. the deposition profile used in JETTO, p_{LH}, is in fact the collisional power p_C, which is shifted in time with respect to p_W. As a result there will be an offset between the modelled and the measured phases. It will be shown in the next section that the larger the time shift between p_C and p_W the higher the CD efficiency is. The current drive j_W in JETTO can be calculated self-consistently by selecting one of the two available Ray-Tracing and Fokker-Planck codes (RT/FP) — FRTC [5] or LHCD [4]. Both codes provide only the steady-state solution for p_{LH}. Moreover the computations are time consuming, which restricts the use of FRTC and LHCD codes in the perturbative simulations. Alternatively, the use of externally defined power deposition profiles with a modulation waveform significantly simplifies and accelerates the JETTO calculations.

The dependencies at the deposition centre are important as they provide important information regarding the absorbed power. Important conclusions as well as essential dependencies can be outlined by means of a simple model in slab geometry [34]. If the modulated localised source heats directly the thermal electrons, as for instance ECRH for which $p_W = p_C$, the phase difference ϕ between T_e and p_C modulations at the deposition maximum varies between $-\pi/4$ for low modulation frequencies $f \to 0$ to $-\pi/2$ for high frequencies $f \to \infty$. In the deposition free region ϕ further decreases and it remains always negative.

The relation between the temperature perturbations and the power deposition profile is discussed here in more detail. Ideally, the amplitude, δT_e, and the phase, ϕ, of T_e modulations are strongly correlated to p_C if one of the following conditions is fulfilled: (*i*) p_C is very narrow and localised, e.g. ECRH heating, or (*ii*) the heat diffusivity, χ_e in equation (4), is constant or very slowly varying function of the plasma radius or the local plasma parameters, e.g. T_e, ∇T_e, etc. None of these conditions

is fully satisfied in the case of LH heating of plasma in which the electron heat transport is determined by turbulence. The LH power deposition profile is broad while the heat flux strongly depends on T_e and $\nabla T_e/T_e$. A number of JETTO runs were performed to study the degree of correlation between p_C and δT_e and ϕ profiles. From the modelling results it was concluded that the phase profile can be used as an approximate indication of the shape of the power deposition profile. In fact the best matches to the experimental data for T_e, δT_e and ϕ was established for p_C profiles which resembles the profile shape of ϕ. The maxima of both, p_C and ϕ, profiles were found to coincide reasonably well, within about 0.1m. An important conclusion from this verification is that basic features of the power deposition profile, e.g. the width and the position of the maximum, can be directly deduced from the phase profile.

3.2. MODELLING OF THE ABSORBED POWER BY 2D FP SOLVER

A basic indication of the expected LH current drive efficiency can be obtained by means of a simple 1D FP model [1]. In this approach, however, the evolution of the bulk electrons is not accounted for as they act as a constant heat sink. Therefore, this model can not be used to assess the energy transfer rate from LH suprathermal electrons to the thermal bulk ones. For that purpose a comprehensive relativistic 2D FP code was developed. The code is similar to the one used in early CD studies as detailed in [35, 36] and was validated by comparison with the examples in these publications. Here the numerical tool is further developed to include the impact of the modulated LH power on the electron heating.

Familiar approach in solving the FP equation is to account for the impact of the RF waves on EDF, f_e, by introducing a RF induced quasilinear flux in the velocity space, characterised by the quasilinear diffusion coefficient D_W. The LH waves produce a flux in the parallel direction in velocity space and consequently change the EDF by forming a plateau. The origin and the extent of this plateau are directly related to D_W shape. For LH waves, which are absorbed via Landau damping, D_W is usually modelled [35] as a constant, D_0, over certain interval in $v_\parallel$ direction. In cylindrical co-ordinates the notations $v_\perp$ and $v_\parallel$ for the perpendicular and parallel velocity component with respect to the magnetic field are adopted, while in normalised velocity units $w=v_\parallel/v_{te}$. The location of the beginning, w_1, and the end, w_2, of this region and the value of D_0 determine the EDF evolution. These parameters will be of main interest as CD efficiency is shown to scale as $j_W/p_W \propto \Delta(w_1+w_2)/2\log(w_2/w_1)$ [36], where the width of the plateau is defined as $\Delta=w_2-w_1$.

As it follows from the theoretical estimates and numerical calculations w_1 usually changes in a narrow range about 3 times the thermal velocity, while according to the linear theory w_2 (or Δ) is strongly coupled to the launched LH wave spectra and is expected to vary in a much broader range. The value of w_1 is related to the largest $N_\parallel$ available at the point of interest and can be assessed by means of RT/FP code. The latter is needed as the $N_\parallel$ spectrum of the launched wave changes significantly towards higher $N_\parallel$ values during the propagation of the LH wave in the plasma. The LHCD code [4] used in JETTO, for instance, gives an irregular D_W profile with $w_1 \approx 2.8$ and $w_2 \approx 9.0$, figure 5a. The value of $w_1 \approx 3$ is also used in other studies on the subject, e.g. [1].

The high velocity end of the plateau, w_2, can be as high as the w value corresponding to the minimum $N_\parallel$ accessible at the investigated region. For an electron temperature of about 700eV, $N_\parallel \approx 1.8$ corresponds to $w_2 \approx 15$. This value is, however, larger than the LHCD code predictions which emphases the fact that the spectrum of the launched wave significantly evolves toward higher $N_\parallel$ before considerable absorption of the wave occurs.

A brief description of the 2D FP code used in the studies is given here. The transient relativistic full 2D equation which describes the evolution of the EDF f_e:

$$\frac{\partial_d f_e}{\partial t} = -\nabla S_p \cdot \mathbf{S} \tag{6}$$

is solved numerically. The momentum p is presented in spherical co-ordinates (p, θ) where p is the absolute momentum and θ is the pitch angle. The velocity $\mathbf{u}$ components are (v, θ) where $v = p/\gamma m_e$. The flux in momentum space $\mathbf{S}$ can be presented as superposition of RF, electric field and collisional contributions, $\mathbf{S} = \mathbf{S_w} + \mathbf{S_E} + \mathbf{S_c}$, whereby $\mathbf{S_w}$ depends on the quasi linear diffusion coefficient:

$$D_w = \frac{D_0, \ w_1 < p_\parallel/\gamma < w_1}{0, \ elsewherw} \tag{7}$$

The absorbed RF power, the power lost due to collisions with thermal electrons and the Joule heating can be computed from the corresponding fluxes:

$$p_W = \int \mathbf{u} \cdot \mathbf{S}_w \, d^3\mathbf{p}; \quad p_C = \int \mathbf{u} \cdot \mathbf{S}_C \, d^3\mathbf{p}; \quad p_E = \int \mathbf{u} \cdot \mathbf{S}_E \, d^3\mathbf{p}; \tag{8}$$

In these calculations the momentum is normalised to $p_{te} = (m_e T_e)^{1/2}$ and the velocity to p_{te}/m_e. In the relativistic case the definition of the thermal velocity slightly differs from the definition given above; however, for temperatures of a few keV the approximation $v_{te} \approx (T_e/m_e)^{1/2}$ is valid. The time is normalised to the collisional time, $\tau = t/\tau_{te}$, with $\tau_{te} = 4\pi\varepsilon_0^2 m_e^2 v_{te}^3/n_e q_e^4 \ln\Lambda$ [37] where $\ln\Lambda$ is the Coulomb logarithm and ε_0 is the dielectric constant of the free space. The power density is normalised to ($n_e m_e v_{te}^2/\tau_{te}$), quasilinear diffusion coefficient D_0 to (v_{te}^2/τ_{te}) and the electric field to $E_{dr} = (m_e v_{te}/q_e\tau_{te})$. The normalised DC electric field, E/E_{dr}, has been assessed in the range 0.001 to 0.003 and its impact on the results of the modelling is small. The transient electromotive force associated with LH driven current being turned on and off has been estimated to vary between zero after the switch on and about twice the DC value when LH CD is switched off. The power absorbed by the bulk electrons p_C, equation (8), can be further used in transport code as shown in figure 4b. The latter deals with the impact of the heat flux on the δT_e evolution and provides the important relation between δT_e and p_C.

In figure 5b the waveforms of $p_W(\tau)$ and $p_C(\tau)$ in three cases with D_0=0.1 and 0.3, w_1=3.0 and Δ=4 and 7 are shown for comparison. The LH power modulation was simulated by changing D_w between 1.67*D_0 and 0.33*D_0 at τ=3800 and 7600, respectively. In this way the whole sequence

forming one period of the modulation with normalised frequency of $f\tau_{te}=2.63\times10^{-4}$ was modelled. The selected parameters match the experimental conditions of #77609, 55.5s, R=3.62m with respect to the modulation frequency (41.67Hz) and depth (67%). The evolution of $p_C(\tau)$ differs from $p_W(\tau)$ shortly after the transient event of switch on or off, figure 5b. The rise and the fall time of the $p_C(\tau)$ waveform are found to depend on w_1, Δ and D_0. The case with the largest plateau width, Δ=7, can be recognised as the one in which $p_C(\tau)$ differs most significantly from $p_W(\tau)$. Increasing D_0 from 0.1 to 0.3 changes mainly the amplitude of the absorbed power, while the shape of $p_C(\tau)$ is modified only slightly. In steady-state condition the power p_C is larger than p_W due to the electric field contribution so that for $\tau\gg1$ the power balance will be $p_W+p_E=p_C$.

A qualitative measure of how the $p_C(\tau)$ waveform changes can be made by means of FFT analysis and comparison of the amplitudes at different harmonics. As the launched power is modulated by a square wave one naturally would use the ratio of the 3rd to the 1st harmonic, noted as $\delta p_{C3}/\delta p_{C1}$, of $p_C(\tau)$ perturbations to quantify the extent to which $p_C(\tau)$ changes with D_w. Simulations for different values of D_0 and plateau parameters, namely w_1 and Δ, were done, figures 5c-e, in order to examine their impact on $\delta p_{C3}/\delta p_{C1}$. In our case the latter decreases when any of the investigated parameters, w_1, Δ and D_0, increase as shown on figures 5c-e. The range of change of $\delta p_{C3}/\delta p_{C1}$ is between 0.3 and 0.2, which is narrower than the region determined by square and triangular waves, for which this ratio is 0.33 and 0.11 respectively. The numerical analysis, figure 5c, shows that the ratio $\delta p_{C3}/\delta p_{C1}$ changes only slightly, about 4%, with w_1 in the range from 2.8 to 3.5. The dependence of $\delta p_{C3}/\delta p_{C1}$ on D_0 is stronger when D_0 is in the range between 0.1 and 0.3, figure 5d. For $D_0>0.3$ the ratio $\delta p_{C3}/\delta p_{C1}$ changes slightly. The RT/FP calculations show that D_w is irregular with average of about 0.2, figure 5a, so that this parameter was assessed more carefully as a result all simulations here were done with values of D_0 of 0.1 and 0.3. It was found that $\delta p_{C3}/\delta p_{C1}$ depends mainly on Δ, figure 5e. It changes from 0.32 to 0.23, or about 30%, for plateau widths of 2 and 6. For comparison D_0 parameter changes this ratio only by about 10%.

The same conclusions can be drawn regarding p_C phase, φ, figure 5f. The strongest dependence is again on the plateau width as the larger Δ is the larger $|\varphi|$ is. From figure 5f it can be concluded that the phase φ can be also used to assess the plateau width.

The impact of the electric field, E/E_{dr}, quasi-linear diffusion coefficient, D_0, and electron temperature, T_e, on the spectral characteristics of δp_C was further assessed by means of other 2D relativistic FP code [38], which includes the trapped particles effects. This is the main difference between the two codes and it is deemed to be of a small importance in our case, as the predictions by the two codes were found very consistent. The results for $\delta p_{C3}/\delta p_{C1}$ and φ versus the normalised modulation period $(f\tau_{te})^{-1}$ are shown in figure 6. Both parameters $\delta p_{C3}/\delta p_{C1}$ and φ are very sensitive to the width of the plateau Δ. It is a reflection of the fact that the collisional energy transfer from the fast to the bulk electrons in the non-relativistic case is roughly proportional to $1/w_2^3$. In the experiments described in this paper the normalised transient electric field varies in the range from 0.0 to about 0.005. It can be seen from figure 6 that the effect of even bigger field, E/E_{dr}=0.01, is

relatively weak. The same conclusion can be made about the effect of the variation of the quasi-linear diffusion coefficient from 0.25 to 0.5. The effect of the temperature variation is pronounced mainly in the case of large w_2 or large plateau width Δ and in the range of higher T_e. The results shown in figure 6 allow us in the future to neglect any possible effect of the electric field on the spectral characteristics of $\delta p_{C3}/\delta p_{C1}$ and φ. Similar conclusions can be made concerning the dependence of $\delta p_{C3}/\delta p_{C1}$ and φ on the value of the D_0 assuming that it is of the order of 0.2-0.5.

3.3. TRANSPORT MODELLING BY MEANS OF CRITICAL $—T_E/T_E$ MODEL

The JETTO code was used to model the modulated LH power heating with the Critical Gradient Model (CGM) [39-42]. In general CGM treats the electron heat flux by assuming that the heat diffusivity, χ_e, increases significantly once the value of $R\nabla T_e/T_e$ exceeds a threshold, called the critical gradient $\kappa_{cr} \equiv R(\nabla T_e/T_e)|_{cr}$. This reflects the fact that in conditions $R\nabla T_e/T_e > \kappa_{cr}$ the electron heat transport is depends mainly on turbulence. Below κ_{cr} the turbulence is suppressed and as a result the residual heat transport is significantly reduced to the level of the gyro-Bohm transport. This can be summarised by the following expression for the heat diffusivity [39]:

$$\chi_e = \chi_0\,\chi_{gB} + \chi_S\,\chi_{gB}\left(- R\,\frac{\nabla T_e}{T_e} - \kappa_{cr}\right) H\left(- R\,\frac{\nabla T_e}{T_e} - \kappa_{cr}\right) \tag{9}$$

where H is a Heaviside function and χ_{gB} is the Gyro-Bohm diffusivity, i.e. it exhibits Gyro-Bohm scaling regarding T_e and magnetic field B; in our case $\chi_{gB} \propto q^{3/2}\,T^{3/2}/B^2$. In addition a dependence on the safety factor, q, is introduced to account for the experimentally observed dependence of the confinement on the plasma current and radial increase of the transport from the core to the edge. The coefficients χ_0 and χ_S quantify the residual and the turbulent transport respectively. The value $\chi_0/\kappa_{cr}\chi_S$ is called the stiffness of the T_e profile.

4. EXPERIMENTAL RESULTS

4.1. AMPLITUDE AND PHASE OF T_E PERTURBATIONS AT DIFFERENT DENSITIES.

The experiments were done at 2.1T-2.3T/1.8MA, 2.7T/1.8MA and 3.4T/1.5MA-1.8MA configurations. Three types of density profiles were selected: low density with central values n_{e0} <2.5-3×10^{19}m^{-3}, moderate or intermediate for which n_{e0} is between 3×10^{19}m^{-3} and 4×10^{19}m^{-3} and high density above 4×10^{19}m^{-3}. Some of the highest density cases were in H-mode plasma with Edge Localised Modes (ELMs) type III edge. During the experiments at 3.4T a number of ECE channels were found noisy and were subsequently removed from the data set thus forming a gap in ECE data between about 3.2m and 3.3m. A comparison to the T_e profiles by the HRTS diagnostic showed consistent profiles by the two diagnostics and that the data in the gap can be approximated by a straight line.

The results of 2.7T/1.8MA experiments are shown in figures 7 and 8. The amplitudes of the T_e modulations are found to have either flat or U -like shape with minima between 3.2m and 3.7m.

Exceptions are the highest density H-mode cases, figure 8 for Pulse No: 73471, when amplitude decreases towards the core. The large uncertainties due to ELMs in this case complicate the analysis.

The phase of the temperature perturbations, ϕ, is always negative which is consistent with the fact that the response of T_e is delayed with respect to the applied modulated power. It was observed that ϕ always decreases with the electron density. The phase maximum is in the plasma core, $R \approx 3.5\text{m-}3.65\text{m}$, in the lowest density case and always moves outward when n_e increases. Transport modelling has also shown that the branch outside of the phase maximum indicates no heating due to LH wave absorption. Therefore it can be concluded that in the example of figure 8, LH absorption is inside about 3.65m for Pulse No: 73473 and about 3.78m for Pulse No: 73417. In the highest density case, Pulse No: 73471, no conclusive statement about the LH deposition from the phase profile can be made.

The density scan at 3.4T is shown in figures 9 and 10. As in 2.7T experiments the amplitudes of the low and intermediate density pulses have minima around 3.4m. At central density $n_{e0} \approx 2 \times 10^{19} \text{m}^{-3}$, Pulse No: 77607, the LH absorption is inside 3.63m while at higher density, Pulse No: 77609, it moves to 3.65m and it reaches 3.73m for $n_{e0} \approx 4.2 \times 10^{19} \text{m}^{-3}$, Pulse No: 77612. The phases increase, i.e. $|\phi|$ decreases, with the density and their maximum moves outward. This can be interpreted as shift of the deposition profile. Particularly interesting here are the high density cases, Pulse No s:77612 and 77616. The density difference is small, about 14% higher in Pulse No: 77616 with $n_{e0} \approx 4.8 \times 10^{19} \text{m}^{-3}$. The amplitudes are however very different, in Pulse No: 77612 δT_e follows the trend similarly to Pulse No s: 77609 and 77611. Temperature modulations are very small in Pulse No: 77616, only narrow region between 3.4m and 3.6m has a signal above the noise level, figure 10. Significant change in phase behaviour is observed as well; maximum $\phi \approx -0.8\text{rad}$ at $R \approx 3.6\text{m}$. Transport calculations of Pulse No: 77616 predict 2 to 3 times larger δT_e if all the coupled LH power is absorbed in the plasma. This observation implies LH power losses causing δT_e reduction, i.e. only a fraction of the coupled LH power enters the plasma and it is eventually absorbed around 3.5m. It was found that $N_{\|\text{acc}}=1.84$ at the location of $R \approx 3.63\text{m}$, where $B \approx 2.8\text{T}$ and $n_e \approx 3.8 \times 10^{19} \text{m}^{-3}$, so that waves with $N_\| < 1.84$ will not propagate inside that point. In order to access the plasma core the LH wave should have minimum $N_\| \approx 1.87$. It can be concluded that the absorbed power actually originates from the fraction of the launched LH wave with $N_\| > 1.84$.

The phase ϕ of the temperature perturbations is always peaked near or at the position of p_{LH} maximum as predicted by the transport modelling. This conclusion was further used to assess the location of the peak of the LH power deposition profile. Figure 11 shows the position of the maxima of the phase ϕ, determined with estimated accuracy of about 0.02m, versus the line averaged electron density $\bar{n}_e$, for a series of pulses at different magnetic fields and densities. Independently of the magnitude of the magnetic field the p_{LH} maximum shifts towards the edge when density increases. At lower density, $\bar{n}_e < 1 \times 10^{19} \text{m}^{-3}$, the power deposition profile is near the core, $R \approx 3.4\text{-}3.6\text{m}$, whilst for $\bar{n}_e > 2.5 \times 10^{19} \text{m}^{-3}$ the maximum of the absorbed LH power is at the very periphery of the plasma, $R > 3.7\text{m}$. The electron temperature was difficult to control, so in the selected points T_e was in the range of $600\text{eV} < T_e < 2\text{keV}$, which may explain the vertical scattering of the points.

14

4.2. COMPARISON WITH THE TRANSPORT MODELLING RESULTS

4.2.1. Steady state profiles

The steady state periods of intermediate and high density pulses at 3.4T were modelled by CGM and the results were compared to the experimental profiles in figure 12. In the calculations the electron density and ion temperature profiles were kept constant, the magnetic equilibrium was computed self-consistently, while the electron temperature was left to evolve in accordance with the CGM model, equations (4) and (9). The CGM model itself does not provide the exact values of χ_0 and χ_S, whilst κ_{cr} can be assessed either theoretically [32] or from the slope of the curve of the perturbed heat flux, $\tilde{q}_e$, versus $R \nabla T_e/T_e$ [39]. The simulations were initially performed by assuming p_{LH} profile with the same shape as ϕ, while χ_0 and χ_S were varied to find the best match between the experimental data and the modelling results. The consistency between the simulations and the measurements was further improved by performing a new series of calculations this time with χ_0 and χ_S fixed as found from the previous step while p_{LH} was slightly modified. In general p_{LH} shape was never changed significantly; however, in some cases, mainly low density pulses, better match to the experimental data was observed with flatter deposition profile, i.e. centre of p_{LH} was shifted inward by 0.1m and the power at the core was increased by 10%.

The best match to the experimental T_e profiles was found for broad off axis power deposition profiles. In all modelled cases the critical gradient value, κ_{cr}, was estimated between 4.5 and 5. The coefficient χ_0 was varied between 0.03 and 0.3 while for χ_S values between 0.7 and 1.75 were found to reproduce best the experimental results. In 3.4T pulses both parameters, χ_0 and χ_S, increase with n_e. The values of χ_0, χ_S and κ_{cr} used in the study are in a good agreement with previous CGM transport modelling results at JET [39]. The consistency between the modelled and experimental electron temperature in all cases in figure 12 confirms the validity of CGM and the implemented power deposition profiles.

4.2.2. Amplitude and phase of electron temperature

The results of the modelled and experimental T_e amplitudes and phases are shown in figure 13. The CGM parameters χ_S, χ_0 and κ_{cr} are the same as in figure 12. In general, δT_{e1} matches reasonably well all the experimental data between 3.3m and 3.7m. The large experimental values of δT_{e1} for $R<3.15$m and $R>3.7$m can not be reproduced. The inconsistency in the core can be explained either by the impact of the sawteeth on electron temperature in that region or by the inability of the CGM to reproduce the electron temperature perturbations in the very core. The edge region, $R>3.7$m in #77609, is not sufficiently optically thick for reliable ECE measurements, thus the δT_{e1} measurements are not considered there.

The phase of T_e perturbations is reproduced reasonably well in the range 3.3m to 3.8m. The experimental, ϕ_{exp}, and the modelled, ϕ_{mod}, phases are always offset and the difference is larger at the lowest density case and smaller at high n_e. The results for the differences between ϕ_{exp} and ϕ_{mod}

are summarised in Table 1. The decrease of the phase offset between the modelled and experimental data, i.e. the quantity $|\phi_{exp} - \phi_{mod}|$, when increasing n_e can be interpreted as an indication that LH power is getting absorbed almost immediately after it is applied. Indeed the lack of phase shift between p_C and p_W at high density implies that heating by LH waves occurs very quickly after its application. As the FP modelling results show, figure 5d, this can be related to a reduction of the plateau width.

In the intermediate density pulses #77609, $B_T=3.4T$ and #73422, $B_T=2.7T$ power deposition profiles from the JETTO s RT/FP codes were investigated as well, figure 14. The differences in modelled and experimental amplitude and phase are apparent and this discrepancy highlights the approximate nature of the power deposition profile given by RT/FP. Too peaked power deposition profiles, figure 14a, clearly indicate that the phase is non-monotonic and each maximum in p_{LH} corresponds to a maximum in ϕ. None of the undertaken experiments has shown such behaviour of ϕ, moreover comparing power deposition profiles in figure 12 and figure 13 it can be concluded that p_{LH} is monotonically decreasing toward the core. The RT/FP code also predicts too narrow depositions, which are closer to the core than the experimental observations, figure 14.

The apparent differences between the RT/FP codes and the experimental results for δT_{e1} and ϕ profiles, figure 14, are thought to be due to the fact that the codes use a simple power spectrum, which is usually approximated by a Gaussian curve centred at $N_{\parallel}=1.84$ and FWHM of about 0.2. In reality the launched LH spectrum consists of many peaks at higher $N_{\parallel}$ as well as small amount of power is launched in negative $N_{\parallel}$ direction. RT/FP code trials with power spectrum, which includes higher $N_{\parallel}$ values, e.g. harmonics of 1.84, resulted in power deposition shift to the plasma edge and p_{LH} profile which is more consistent with the observed δT_{e1} and ϕ profiles. At the moment the launched power spectrum can not be measured precisely, which is a real drawback regarding the use of RT/FP codes for power deposition calculations.

4.2.3. Relation between δT_{e3} / δT_{e1} and δp_{C3} / δp_{C1}

If the power is modulated with the same amplitude but at different frequencies the temperature perturbations at the higher frequency will have lower amplitude. In the deposition free region the oscillations at higher frequencies will be even further suppressed. This can be thought as a way to tell the LH power deposition profile; indeed if the modulation is at high enough frequency δp_C and δT_e profiles will tend to be closer as from equ. (5) it follows that $-3/2i\omega n_e T_e = p_c$.

Transport simulations were performed in order to investigate the impact of the transport on δT_e at different frequencies. A scan of the modulation frequency f shows that for $f>200Hz$ the ratio $f n_e \delta T_e / \delta p_C$ and the phase of the temperature perturbation ϕ at the deposition maximum do not change with f. The latter has an asymptotical value of $-\pi/2$, while from equation (5) it is easily to conclude that $f n_e \delta T_e / \delta p_C \approx const$ if the transport and the losses have negligible impact at high frequency. If square waveform is used for modulations and f is sufficiently high then the ratio of the 3rd to the 1st harmonics of δT_e and δp can be approximated by the formula $3\delta T_{e3}/\delta T_{e1} \approx \delta p_{C3}/\delta p_{C1}$.

At lower frequencies, $f<100$Hz, however, ϕ and the ratio $fn_e\delta T_e/\delta p_C$ change with f. The phase approaches $-\pi/4$ for very low frequencies whilst $fn_e\delta T_e/\delta p_C$ is not a constant anymore as indicated by the transport modelling. Simulations with JETTO were done to investigate the ratio $C=(\delta p_{C3}/\delta p_{C1})/(\delta T_{e3}/\delta T_{e1})= (\delta T_{e1}/\delta p_{C1})/(\delta T_{e3}/\delta p_{C3})$, figure 15. It relates the amplitudes of the measured δT_{e1} and δT_{e3} to the amplitudes of the source, δp_{C1} and δp_{C3}, which in turn can be compared to the results of the 2D FP simulations. The ratio $\delta p_{C3}/\delta p_{C1}$ in the case of square modulation it is 0.3 so C profile differs from $\delta T_{e1}/\delta T_{e3}$ by this factor only. As the theory predicts C is minimum near the deposition maximum and away from it further increases as a result of the stronger damping of the higher harmonics in the plasma.

The conclusions made here are valid near the deposition centre only, where the heat source is greater than the diffusive losses. Outside of the deposition centre, where heat source is smaller this ratio can vary significantly.

4.3. ESTIMATE OF THE CD EFFICIENCY

The conclusions from the JETTO modelling regarding the impact of the transport on T_e perturbations are used in this particular case to find the relation between the ratio of $\delta T_{e3}/\delta T_{e1}$ and $\delta p_{C3}/\delta p_{C1}$. As shown in previous section $\delta p_{C3}/\delta p_{C1} = C(\delta T_{e3}/\delta T_{e1})$ and the constant C can be derived from the transport simulations, figure 15.

The plateau width, Δ, is assessed via comparison, figure 16a, of the FP results for $\delta p_{C3}/\delta p_{C1}$ and experimental data for $C\delta T_{e3}/\delta T_{e1}$ as C was derived from the transport simulations. The accuracy in $f\tau_{te}$ is assessed to be about 15% for Pulse No: 77609 in which pulse TS LIDAR data were used, while in Pulse No: 77612 HRTS density profiles provide better estimate of the collision time resulting in $f\tau_{te}$ accuracy of about 12%. The values of $C\delta T_{e3}/\delta T_{e1}$ in figure 16a are plotted with error bars from the standard deviation of δT_{e1} and δT_{e3} amplitudes. The experimental results were taken in two points near the deposition maxima and indicate large plateau, $\Delta\geq6$ and consequently significant CD efficiency for Pulse No: 77609 with electron density $n_e(3.6m) \approx 2\times10^{19}\text{m}^{-3}$, figure 16a. At higher density $n_e(3.6m)\approx3\times10^{19}\text{m}^{-3}$ in Pulse No: 77612, the value of $C\,\delta T_{e3}/\delta T_{e1}$ was found consistent with FP results for small plateau width, $\Delta\approx2$. This implies certain reduction of the CD efficiency.

These conclusions are supported by the results for the phases, figure 16b. The experimental data for $\phi_{exp}-\phi_{mod}$ in the lower density Pulse No: 77609 fit well to the expected phase, φ, of $\tilde{p}_{C1}$for $\Delta\approx6$, while the lower values of $|\phi_{exp}-\phi_{mod}|$ in Pulse No: 77612 match the FP results for $\Delta\approx2$. These conclusions qualitatively agree with the dependencies found from the analysis of the amplitudes, figure 16a. The errors in phase are assumed to be of the order of the errors in the amplitude, i.e. about 20%. The slight difference between the data matches for the phases and amplitudes can be explained with lower accuracy of the experimental phase. This is mainly due to the non sufficient time resolution of the P_{LH} signal which is used as a reference for ϕ_{exp}.

The results from JET pulses at 2.1T-2.3T, 2.7T and 3.4T with modulated LH power are summarised in figure 17. It compares the experimental data for $C\delta T_{e3}/\delta T_{e1}$ and $\phi_{exp}-\phi_{mod}$ with an average values

of $C=3$ and $\phi_{mod}=-1.1$rad to the results for $\delta p_{C3}/\delta p_{C1}$ and ϕ from the relativistic 2D Fokker-Planck code [38]. Independently, on the magnetic field, figure 17, all the experimental data are between $\Delta=2$ and $\Delta=6$. The error bars of the measurements are about 20% for $C\delta T_{e3}/\delta T_{e1}$ and $\phi_{exp}-\phi_{mod}$ and 15% for $f\tau_{te}$. The pulses at very low density, for which $(f\tau_{te})^{-1}<1000$, are not shown in the graph as the theoretical curves coalesce for lower values of $(f\tau_{te})^{-1}$. In order to assess the CD efficiency for very low density pulses the modulation frequency f should be reduced. However, one should take into account that at very low frequency the heat transport is dominant in T_e evolution.

More detailed picture of the CD efficiency dependence on the plasma density is shown in figure 18 [20]. The ratio $\delta T_{e3}/\delta T_{e1}$ and the phase ϕ_{exp} are deduced from the measurements at the position of ϕ_{exp} maximum. Solid symbols correspond to $\delta p_{C3}/\delta p_{C1}$ and ϕ as calculated by the FP code [38] assuming that $w_1=3$ and $w_2=c/(N_{\parallel acc}v_{te})$, with $N_{\parallel acc}$ defined by the local accessibility condition, equation (3), at the peak of the power deposition profile. It should be noted that the selected upper limit of the plateau $w_2=c/(N_{\parallel acc}v_{te})$ corresponds to the assumption that LH waves experience multiple pass absorption. This regime of absorption is predicted by the ray tracing and Fokker-Planck modelling in the case of relatively low T_e (a few keV) and small launched $N_{\parallel}$ spectrum ($N_{\parallel}<2$). The launched waves in this regime bounce many times in $N_{\parallel}$ (or phase velocity $c/N_{\parallel}$) space. At the higher end they reach such $N_{\parallel}$, that enable effective absorption of the waves. It happens, when the parallel phase velocity of the wave is reduced to the level of $v_{\parallel}=c/N_{\parallel}\approx 3v_{te}$, i.e. $N_{\parallel}$ increases to $c/3v_{te}$. In the lower end the parallel phase velocity may increase up to the limit defined by the local accessibility condition, namely equation (3). This is the highest velocity or the lowest $N_{\parallel}$ allowed at certain position in the plasma. Calculated in this way the $N_{\parallel}$ spectrum provides the highest possible CD efficiency. In addition in 3.4T case $\delta p_{C3}/\delta p_{C1}$ and ϕ are calculated in two particular cases for different values of w_2 as shown by the circle symbols in figure 18b.

The x symbols in figure 18 show the average experimental values for $C\delta T_{e3}/\delta T_{e1}$ and $\phi_{exp}-\phi_{mod}$. The vertical bars indicate the upper and the lower limits of $C\delta T_{e3}/\delta T_{e1}$ and $\phi_{exp}-\phi_{mod}$ for C in the range from 2.6 to 3.1 and ϕ_{mod} from -0.9rad to -1.3rad. Horizontal error bars are the accuracy in the line averaged density measurements.

The results of the FP modelling at low density are within the range of the measured $C\delta T_{e3}/\delta T_{e1}$ and $\phi_{exp}-\phi_{mod}$. At higher n_e however, the measured values are well above the modelled ones and the discrepancy increases with increasing density. At high density best agreement is reached at the lowest w_2, $w_2=5$ (or $\Delta=2$) in figure 18b, which corresponds to the lowest current drive efficiency.

CONCLUSIONS

The experimental study presented here suggests a new method for assessment of the LH deposition and LH CD efficiency. FP and transport simulations were exclusively used to investigate the fundamental dependencies and to process the experimental data. The new technique relies on application of modulated LH power and FFT analysis of the ECE measurements. Transport simulations featuring Critical Gradient Model [39] were used first to estimate the LH deposition

profile. The transport modelling results were also used to find the relation between the pairs $\delta T_{e3}/\delta T_{e1}$ and ϕ and $\delta p_{C3}/\delta p_{C1}$ and φ. Here $\delta T_{e3}/\delta T_{e1}$ and ϕ are the ratio of the amplitudes of the 3rd and 1st harmonics and the phase at the main harmonic of T_e perturbations, while $\delta p_{C3}/\delta p_{C1}$ and φ are the corresponding quantities with respect to the LH collisional power. The latter were found strongly related to the width of the plateau of the Electron Distribution Function created by the LH waves, hence $\delta p_{C3}/\delta p_{C1}$ and φ were used to assess the CD efficiency.

The LH power deposition profiles were found to be broad off-axis and with their maximum located in the vicinity of the maximum of ϕ. The latter shifts towards the edge when plasma density increased. In the highest density cases when the density at the edge approached accessibility limit [27, 28] the character of the temperature perturbation testifies that only a part of the launched LH power was absorbed in the plasma. When the density was above the accessibility limit, a significant part of the LH power was lost beyond the separatrix. This observation confirms the importance of the accessibility condition for the assessment of the heating and current drive efficiency.

The experimental values of $\delta T_{e3}/\delta T_{e1}$ and ϕ confirm that at the plasma density well below the accessibility limit large CD efficiency can be associated with large plateau of the distribution function, i.e. plateau width of $\Delta \approx 6$. At higher densities the CD effects are reduced as the experimental data are consistent with modelling results for smaller plateau, $\Delta \approx 2$. The dependence of CD efficiency on the plasma density was demonstrated for 2.1T-2.3T and 3.4T pulses. The results from two independent FP codes are consistent and clearly show reduction of the CD efficiency at higher densities. The degradation of CD efficiency decrease with density is consistent with anomalously high rate of the parallel refractive index $N_\parallel$ increase in the vicinity of the launcher.

Results of Ray Tracing and Fokker-Planck (RT/FP) modelling were found inconsistent with the experimental data. The discrepancy becomes greater with the rise of the plasma density. It is thought that the mismatch between RT/FP calculations and experimental results is due to the idealised power spectrum used in the RT/FP codes. In reality LH wave is launched in the plasma with spectrum rich of high $N_\parallel$ components.

REFERENCES

[1]. N. Fish, 1987, *Rev. Mod. Physics* **59** (1), p.175

[2]. M. Brambila, 1976, *Nucl. Fusion* **16**, p.47

[3]. P. Boloni, 1985, Wave Heating and Current Drive in Plasmas, eds. V Granatstein and P. Colestock, (Gordon and Breach Sci. Publishers, 1985), p.175 and references therein

[4]. Y. Baranov *et al*, 1996, *Nucl. Fusion* **36**, p.1031

[5]. A. Esterkin, A. Piliya, 1996, *Nucl. Fusion* **36**, p.1501

[6]. A. Smirnov, R. Harwey, 1995, *Bull. Am. Phys. Soc.* **40**, p.1837

[7]. R. Devoto *et al*, 1992, *Nucl. Fusion* **32**, p.773

[8]. F. Imbeaux, Y. Peysson, 2005, *Plasma Phys. Contr. Fusion* **47**, p.2041

[9]. P. Boloni, 1986, *Phys. Fluids* **29**, p.2937

[10]. P. Boloni *et al*, 1998, Benchmarking of lower hybrid current drive codes with application to ITER relevant regimes, in IAEA, *Plasma Physics and Controlled Nuclear Fusion Research*, pp. IT/P1—2, Chengdu, China, 1998, IAEA

[11]. J. Wright *et al*, 2005, *16th Topical Conference on RF Power in Plasmas*, eds. J. Wukitch and P. Boloni, Park City, Utah, 2005, AIP Conference Proceedings 787, p.287

[12]. ITER Physics expert group, 1999, *Nucl. Fusion* **39**, p.2495

[13]. C. Gormezano *et al,* ITER Physics expert group, 2007, *Nucl. Fusion* **47**, p.S285

[14]. W. Hooke, 1984, *Plasma Phys. Contr. Fusion* **26**, p.133

[15]. D. Start, 1983, Non-Inductive Current Drive in Tokamaks, Proc. IAEA Technical Committee Meeting, Culham, UK, 18-21 Apr. 1983

[16]. M. Brusati *et al*, 1994, *Nucl. Fusion* **34**, p.23

[17]. K. Kirov *et al*, 2002, *Plasma Phys. Contr. Fusion* **44**, p.2583

[18]. E. Lerche, D. Van Eester *et al*, 2008, *Plasma Phys. Contr. Fusion* **50**, p.035003

[19]. Y. Peysson, 1993, *Plasma Phys. Contr. Fusion* **35**, p.B253

[20]. Y. Baranov, K. Kirov *et al*, 2009, *18th Topical Conference on RF power in Plasma*, Gent, Belgium, 2009

[21]. K. Kirov, Y. Baranov *et al*, 2009, 36th ESP Conference on Plasma Physics and Controlled Nuclear Fusion, Sofia, Bulgaria, 2009

[22]. M. Pain *et al*, 1989, Proc. 13th Symp. on Fusion Engineering (Knoxville, TN)

[23]. M. Lennholm *et al*, 1995, Proc. 16th Symp. on Fusion Engineering (Champaign, IL)

[24]. E. de la Luna *et al*, 2004, Recent Development of ECE Diagnostics at JET , 13th Joint Workshop on Electron Cyclotron Emission and Electron Cyclotron Resonance Heating, Nizhny Novgorod, Russia, May 17-20, 2004

[25]. C. Gowers *et al*, 1995, Rev Sci Instrum **66**(1), p. 471

[26]. C. Sozzi *et al*, 2009, *18th Topical Conference on RF power in Plasma*, Gent, Belgium, 2009

[27]. T.H. Stix, 1962, The Theory of Plasma Waves, (McGraw-Hill, Inc., New York, 1962)

[28]. V.E. Goland, 1972, *Sov. Phys. Tech. Phys.* **16**, p.1980

[29]. I. Shkarofsky, 1999, *J Plasma Physics* **61**, p.107

[30]. H. A. Gaberson, 2006, *Sound and Vibration*, p.14

[31]. W. Horton, 1999, *Rev. Mod. Phys* 7**1**, p.735

[32]. J. Connor, H. Wilson, 1994, *Plasma Phys. Contr. Fusion* **36**, p.719

[33]. G. Cenacchi, A. Taroni, 1988, JETTO: A free-boundary plasma transport code (basic version) , JET report, JET-IR(88)03

[34]. F. Leuterer *et al*, 2003, *Nucl. Fusion* **43**, p.744

[35]. C. Karney, 1986, Comp. Phys. Rep. 4(3-4), p.182

[36]. C. Karney, N. Fish, 1979, *Phys. Fluids* **22**(9) p.1817

[37]. J. Huba, 1994, NRL Plasma Formulary, p.31

[38]. M. Shoucri, I. Shkarofsky, 1994, *Comput. Phys. Comm.* **82**, p.287

[39]. P. Mantica *et al*, 2008, *Fusion Science and Technology* **53**, p.1152

[40]. X. Garbet, 2004, *Plasma Phys. Contr. Fusion* **46**, p.1351

[41]. F. Ryter *et al*, 2003, *Nucl. Fusion* **43**, p.1396

[42]. F. Imbeaux *et al*, 2001, *Plasma Phys. Contr. Fusion* **43**, p.1503

JET Pulse No:	Model		At R max p_{LH}		At 3.6m		At 3.4m	
	R max ϕ_{mod}, m	R max p_{LH}, m	ϕ_{mod}, rad	ϕ_{exp}-ϕ_{mod} rad	ϕ_{mod}, rad	ϕ_{exp}-ϕ_{mod} rad	ϕ_{mod}, rad	ϕ_{exp}-ϕ_{mod} rad
77607	3.61	3.53	-1.30	-0.83	-1.23	-0.87	-1.48	-0.82
77609	3.64	3.64	-1.17	-0.28	-1.21	-0.25	-1.54	-0.20
77611	3.68	3.69	-1.10	-0.21	-1.21	-0.14	-1.56	-0.16
77612	3.73	3.71	-0.93	-0.20	-1.11	-0.14	-1.51	-0.05

Table 1. Experimental, ϕ_{exp}, and modelled, ϕ_{mod}, phases and their difference for JET Pulse No's: 77607, 77609, 77611 and 77612. The positions of the maxima of ϕ_{mod} and p_{LH} from JETTO simulations are given in columns 2 and 3. The maximum of ϕ_{exp} is approximately at the same position as the corresponding ϕ_{mod} peak.
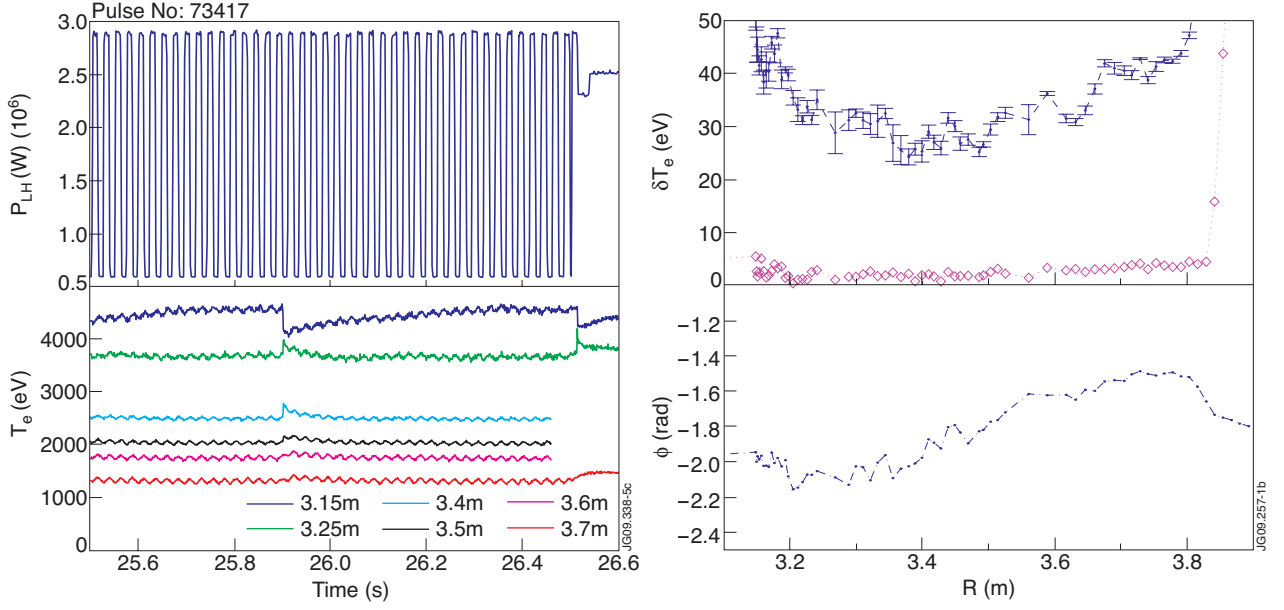
Figure 1: Time traces of the total LH power, P_{LH}, modulated with 41.67Hz and selected KK3 channels (a); the amplitude of the 1st (dots) and 3rd (diamonds) harmonic and phase of the 1st (dash-dotted line) harmonic (b). FFT is done in time interval 25.5s to 26.46s. The large error bars inside R=3.4m are result of the sawtooth at t≈25.9s, whilst the ECE data for R>3.83m are not reliable due to the insufficient optical thickness at the edge.
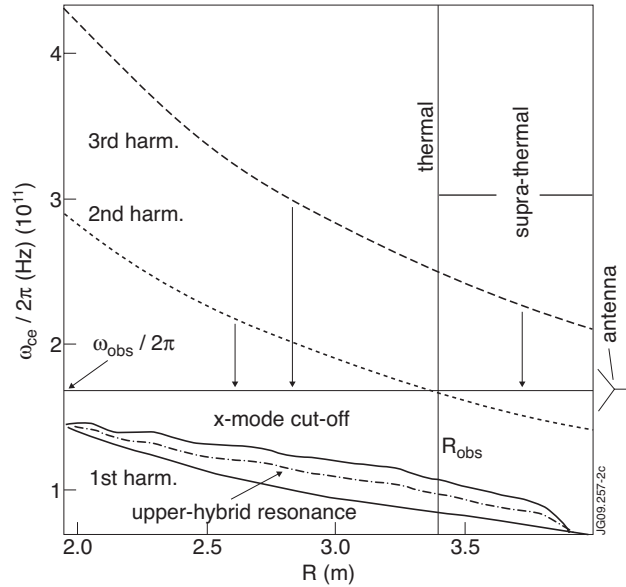
Figure 2: Radial dependence of the 1st, 2nd and 3rd harmonics of the cyclotron resonance frequency ω_{ce}. The magnetic field and density correspond to 3.4T JET Pulse No: 77612. The 2nd and the 3rd harmonic emission produced in the region $R<R_{obs}$ by energetic electrons downshifted to the observation frequency ω_{obs} is reabsorbed by thermal electrons in the vicinity of $\omega_{obs} = 2\ \omega_{ce}$ layer. Emission produced in the region of $R>R_{obs}$ at the 3rd harmonic downshifted to ω_{obs} escapes the plasma without being re-absorbed and can be registered by receiving antenna, which is shown schematically at the separatrix location.
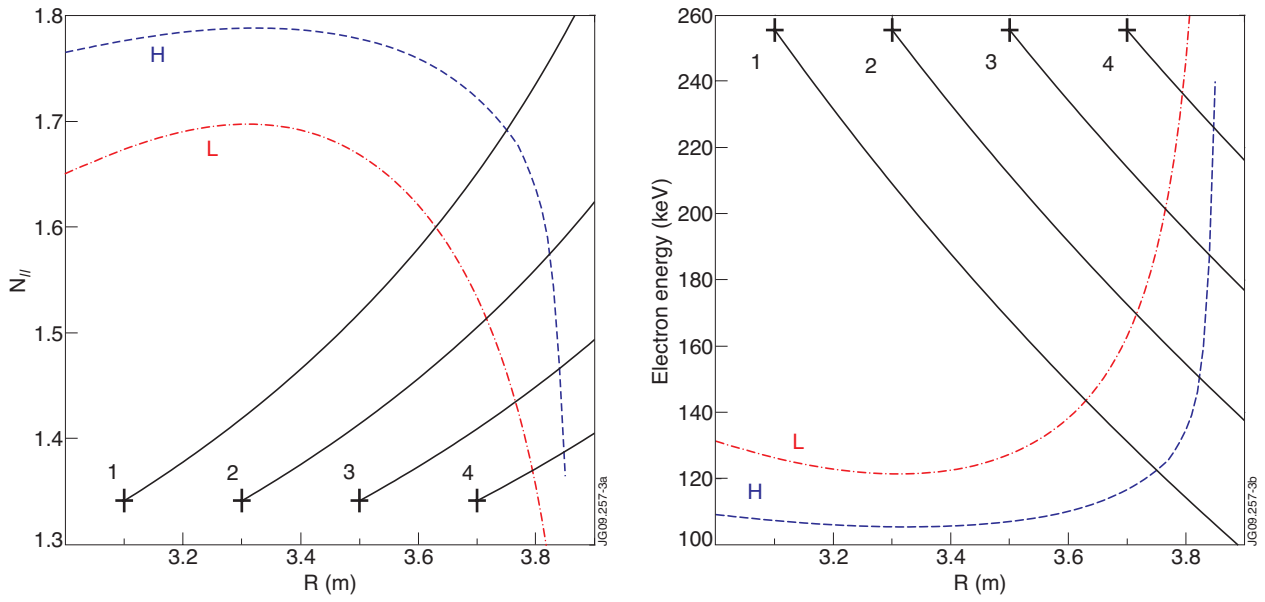
Figure 3: The phase diagrams ($N_{//}$, R) (a) for LH waves (solid lines), which accelerate electrons emitting at four different ω_{obs}. The corresponding R_{obs} are indicated by crosses numbered 1 to 4. The minimum possible $N_{//}$ vs. R as defined by the accessibility condition (3) is plotted for two 3.4T JET pulses at different densities Pulse No's: 77612, $n_{e0} \approx 4.2 \times 10^{19} m^{-3}$ (H dashed line in blue) and 77609, $n_{e0} \approx 3.2 \times 10^{19} m^{-3}$ (L dash dotted line in red), respectively. Below L- and H-lines the acceleration of the fast electrons emitting at $\dots_{obs}$ is impossible as the propagation of corresponding LH waves is not allowed by the accessibility condition (3). The phase diagrams (E_e, R) of electrons emitting at the same four frequencies ω_{obs} is given in (b). The maximum possible energy, see (2) and (3), vs. R for electrons accelerated by LH waves for the reference pulses given in (a) are indicated by L- and H-lines. The lines below the L- and H-line in (b) show E_e and R of the fast electrons, which are allowed to interact with the LH waves. The phase curves ($N_{//}$, R) above the L- and H-line in (a) indicate a region for each pulse, respectively, where the acceleration is impossible due to absence of LH waves with sufficiently high phase velocity.
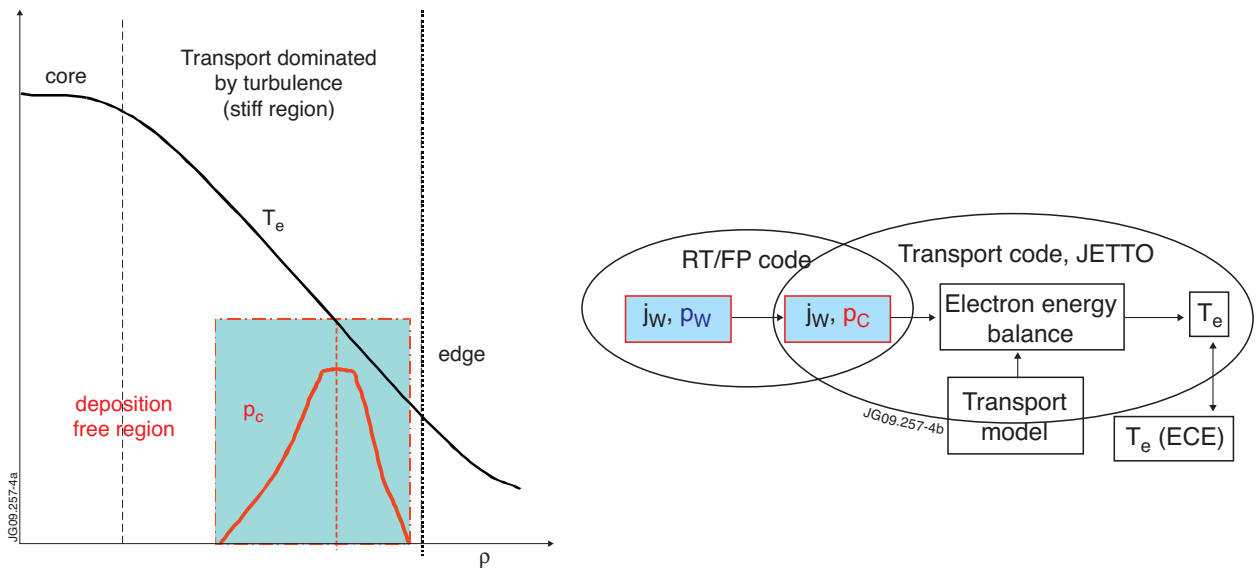
Figure 4. Sketch of the plasma cross section showing typical regions regarding power deposition (in red) and electron temperature (in black) profiles (a) and a sketch of the integrated modelling, RT/FP and transport code (b).

23
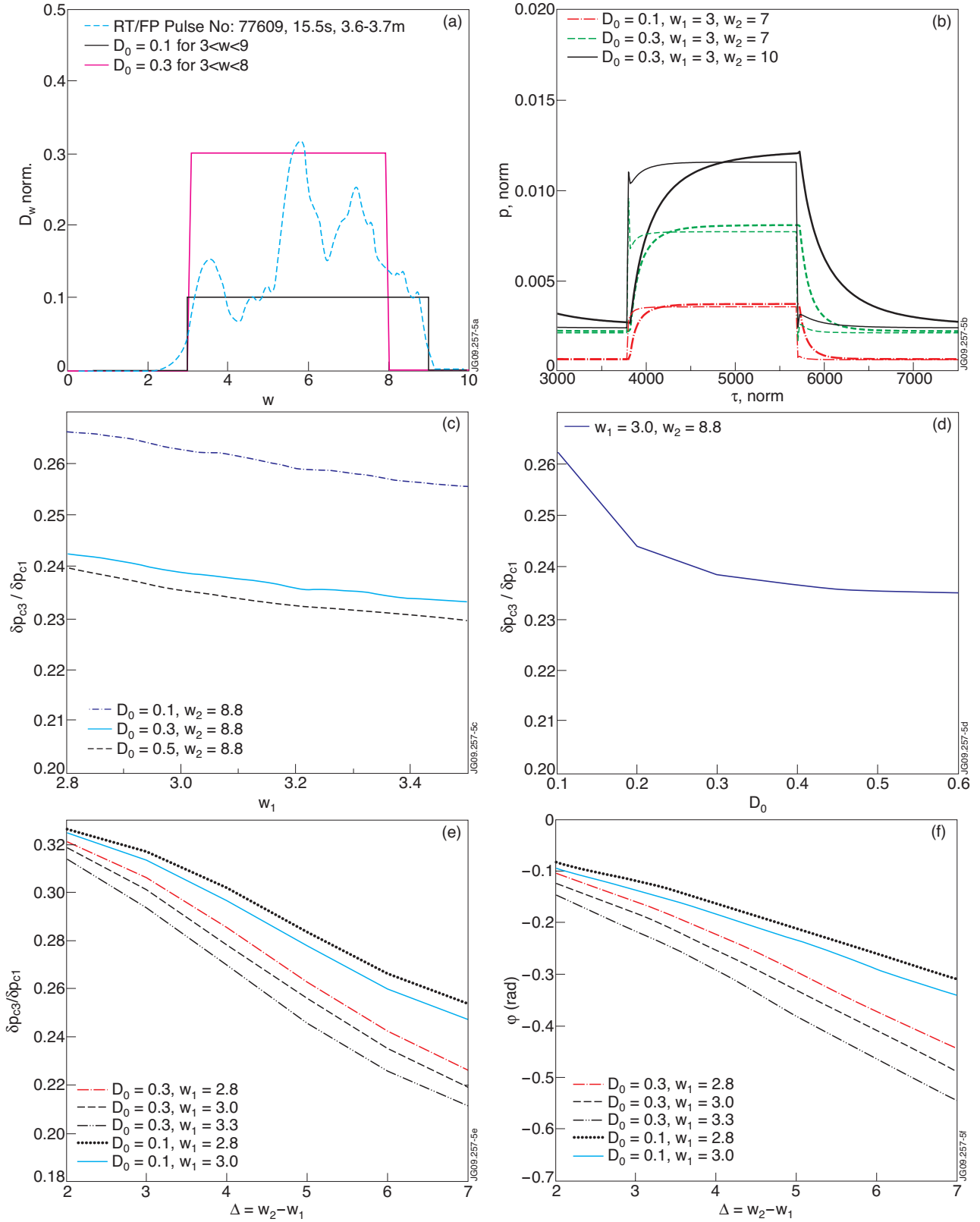
Figure 5: Quasilinear diffusion coefficient D_0 for intermediate density JET Pulse No: 77609, 15.5s, 3.6m-3.7m, as given from LHCD code [4] and example profiles used in the study (a). Results for p_W (thin line) and p_C (thick line) power waveforms at different D_0 and D (b) as derived from FP modelling with $w_1 = 3$, $E/E_{dr} = 0.002$, $T_e = 700eV$, LH power on at $t = 3800$ and off at $\tau = 5700$ corresponding to modulation at normalised frequency of 2.63×10^{-4} and modulation depth of 67%. Dependence of the ratio $\delta p_{C3}/\delta p_{C1}$ on w_1, D_0 and Δ (c,d,e). The dependence of φ on w_1 and D_0 is shown in (f). The phases in (f) were derived by adding $+\pi/2$ to the results of FFT analysis as the phase shift of the first harmonic of the square waveform is $-\pi/2$
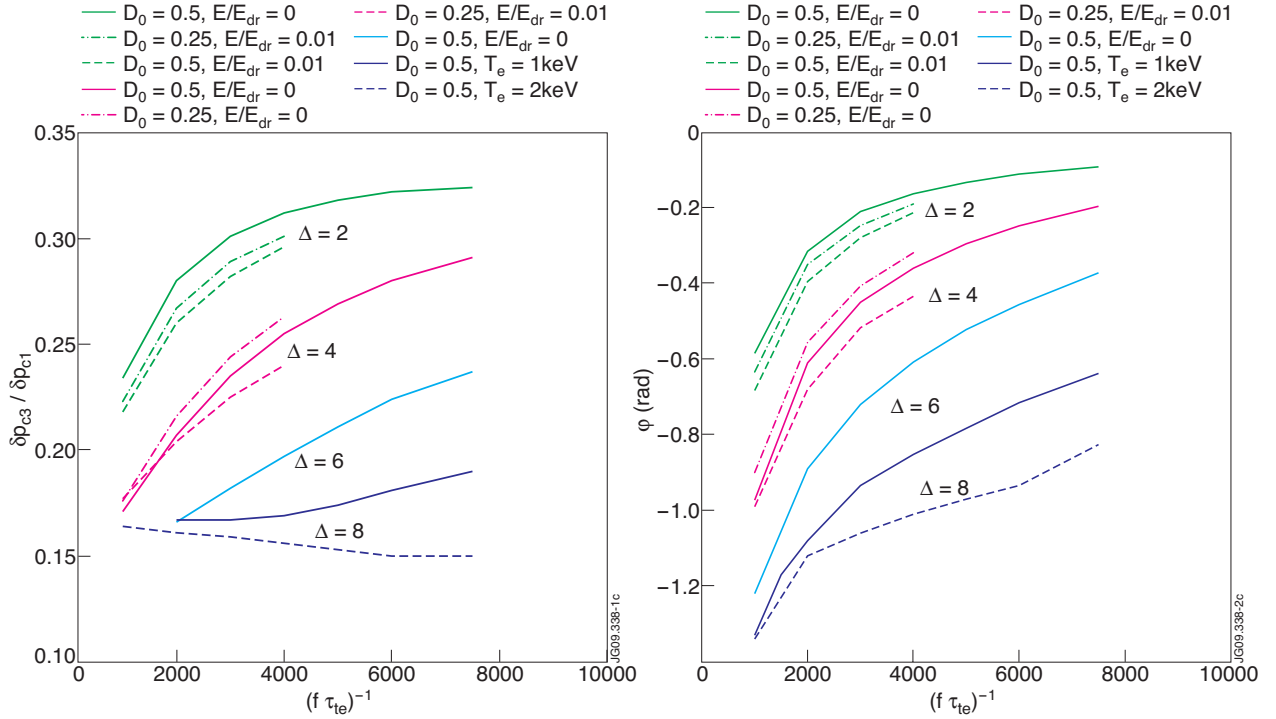
Figure 6: The ratio $\delta p_{C3}/\delta p_{C1}$ (a) and the phase φ (b) versus normalised modulation period $(f\tau_{te})^{-1}$ as derived by the 2D Fokker-Planck code [38]. In the simulations the plateau origin was at $w_1=3.5$ while the modulation depth was 100% and all cases except the last one were with $T_e=1keV$. The corresponding plateau widths, Δ, are shown in the graph while the parameters E/E_{dr}, D_0, and T_e are given in the legend.
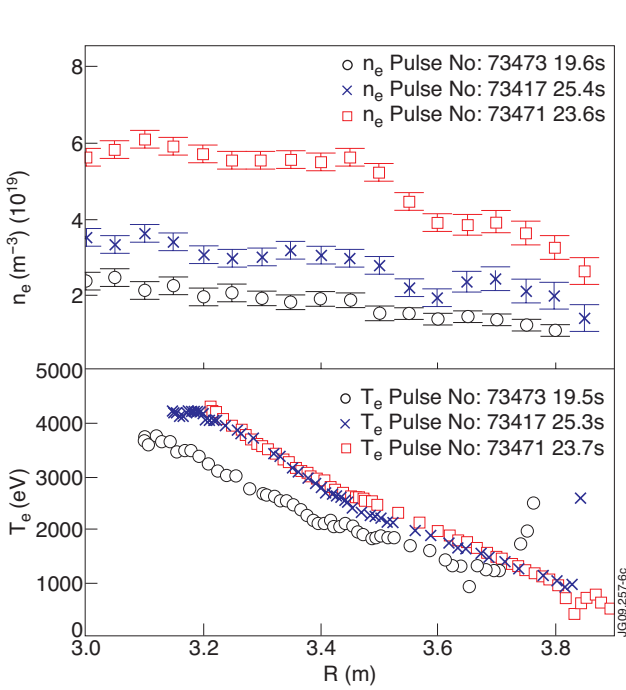
Figure 7. Density and electron temperature profiles for 2.7T series of pulses. Highest accessible density for $N_{//}=1.8$ is about 3×10^{19} m^{-3}. The largest density case, Pulse No: 73471, is in H-mode.
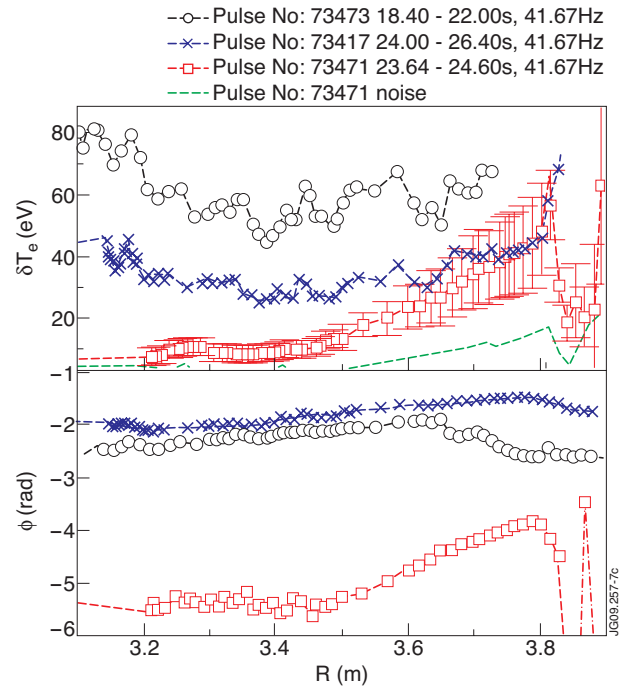
Figure 8. Amplitude and phase of T_e perturbations for the selected three cases in figure 7. The large errorbars in Pulse No: 73471 are due to the impact of the ELMs.
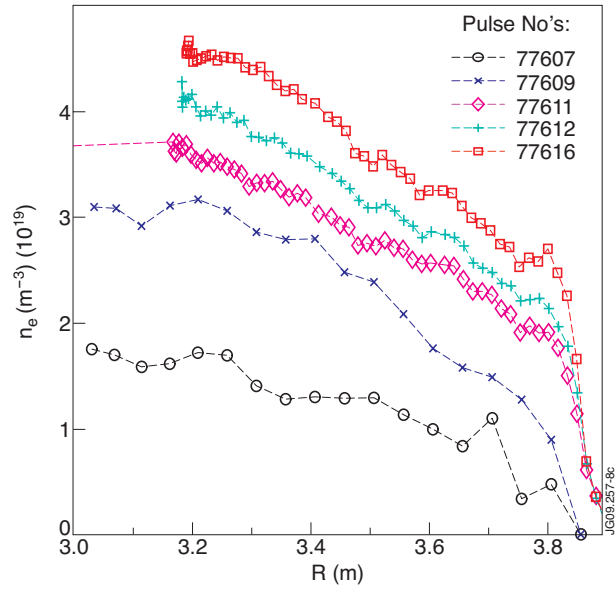
Figure 9: Density profiles for 3.4T series of pulses. Low density data, Pulse No's: 77607 and 77609, are measured by LIDAR TS, whilst for the remaining HRTS was used. The largest density case, Pulse No: 77616, is in H-mode. The accessibility of LH wave with $N_{//}=1.8$ in Pulse No: 77616 is up to R=3.73m.
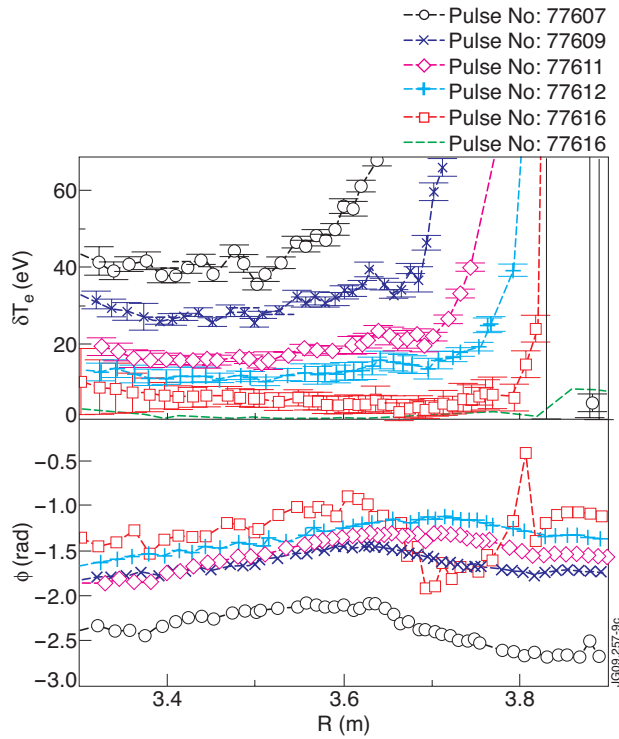
Figure 10: Amplitude and phase of T_e perturbations for the selected five cases in figure 9. The uncertainties in the amplitude are assessed via the spectrogram method, window of 0.1s and shift of 0.0024s.
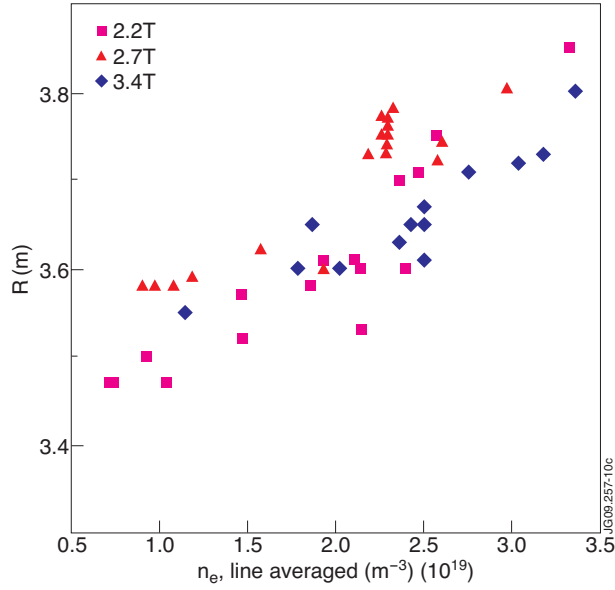
Figure 11: Position of maximum of the phase f vs. line averaged density $\overline{n}_e$. The peak of p_{LH} is located near the maximum of ϕ.
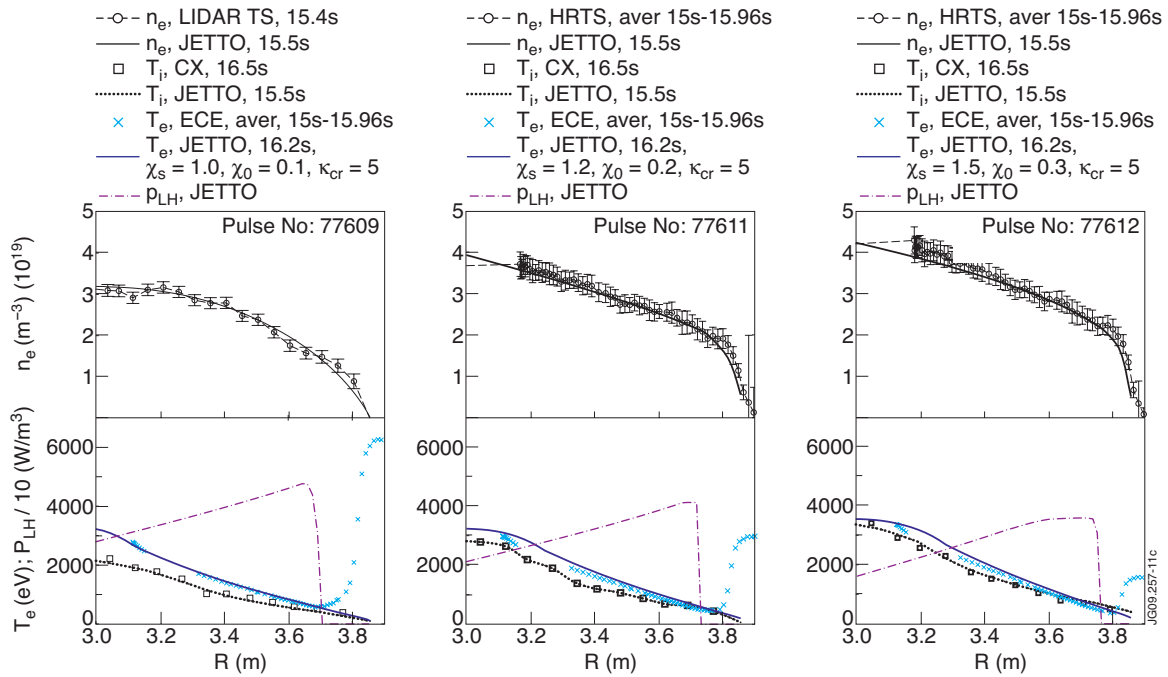
Figure 12. JETTO simulation of the steady state 3.4T/1.5MA plasma at intermediate density (a) and 3.4T/1.8MA intermediate (b) and high density (c) pulses. The smoothed (solid lines) and experimental ('o' points and dash line) density profiles are given on the top graph. The ion temperature profiles, smoothed (dotted lines) and experimental by Charge Exchange measurement (squares) are on bottom graph. The ECE data ('x' sign) and the modelled T_e profiles (solid lines) with the corresponding power deposition profiles p_{LH} (dash-dotted line) are given on the bottom graph. The values of χ_S, χ_0 and κ_{cr} used in CGM are indicated in the legends.
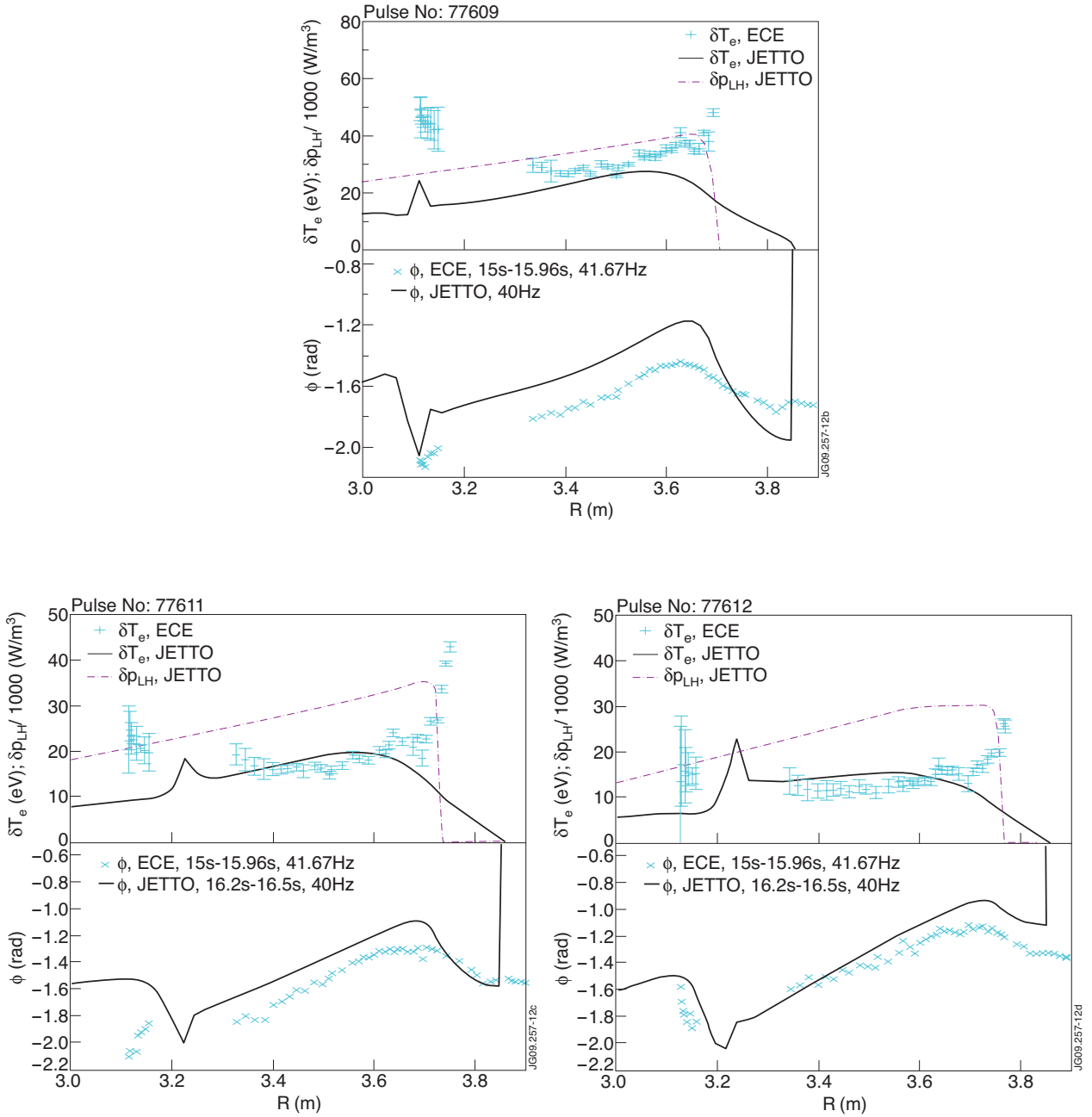
Figure 13: Amplitude (above) and phase (bottom) of T_e perturbations as modelled by JETTO compared to the experimental data in 3.4T/1.5MA intermediate (a), 3.4T/1.8MA intermediate (b) and high (c) density plasma. The modelling results are given by solid lines, while the experimental data are displayed by '+' and 'x' symbols. The modulated power deposition profiles, δp_{LH}, are given in kW/m³ on the top graph. The modulation frequencies and the FFT time windows are indicated in the bottom legends.
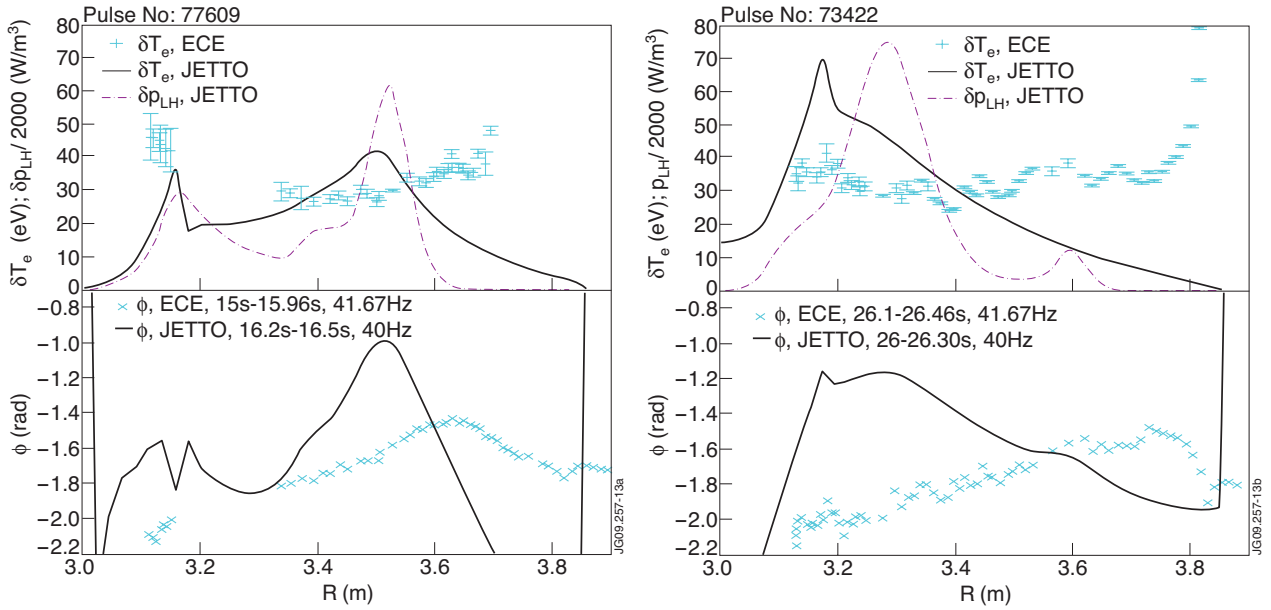
Figure 14. JETTO calculations of amplitude (top graph, solid line) and phase (bottom graph, solid line) compared to the experimental data ('+' and 'x' signs) for the intermediate density Pulse No's: 77609 (a) and 73422 (b). Modulated power deposition profiles, δp_{LH}, (top graph, dash dotted line) were selected to be either the LHCD code result (a) or FRTC (b) output.
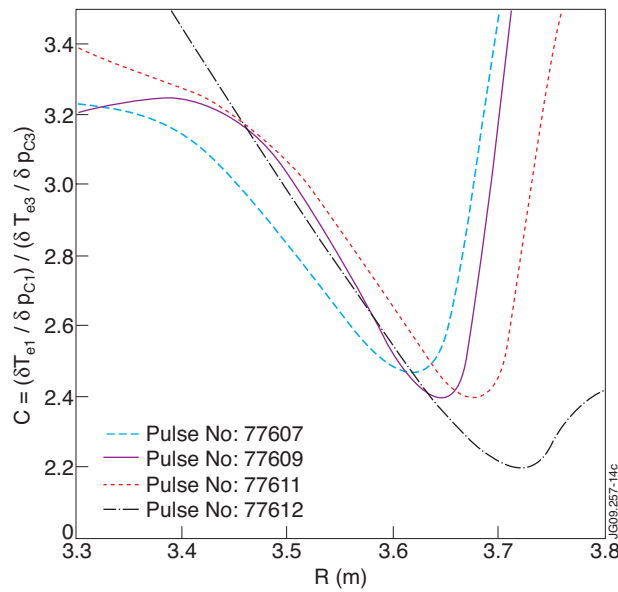

Figure 15. $(\delta T_{e1}/\delta p_{C1})/(\delta T_{e3}/\delta p_{C3})$ profile from JETTO calculations. The power deposition profiles are given in figure 13 by dash-dotted lines.
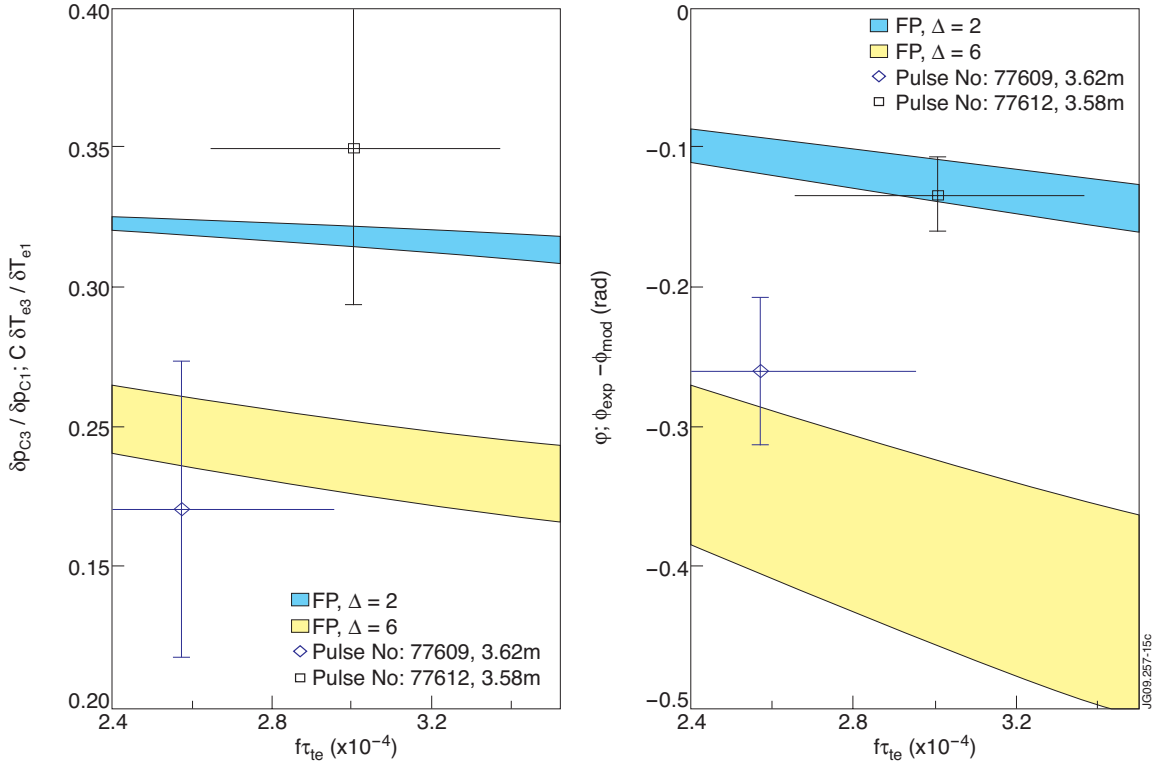
Figure 16: The ratio $\delta p_{C3}/\delta p_{C1}$ (a) as modelled by 2D FP code with $w_1=3$, $E/E_{dr}=0.002$, $T_e=0.7keV$ and for $\Delta=2$, $D_0=0.1-0.3$ (cyan region) and $\Delta=6$, $D_0=0.1-0.3$ (yellow region) versus $f\,\tau_{te}$ compared to the ratio $C\,dT_{e3}/\,d\,T_{e1}$ from experimental measurements in Pulse No's: 77609 at 3.62m (blue diamond) and 77612 at 3.58m (black square). The constant C is determined from transport modelling and given in figure 15. The phase difference $\phi_{exp}-\phi_{mod}$ (b) for Pulse No's: 77609 (blue diamond) and 77612 (black square) is compared to p_C phase φ as derived from 2D FP code for $\Delta=2$, $D_0=0.1-0.3$ (cyan region) and $\Delta=6$, $D_0=0.1-0.3$ (yellow region).
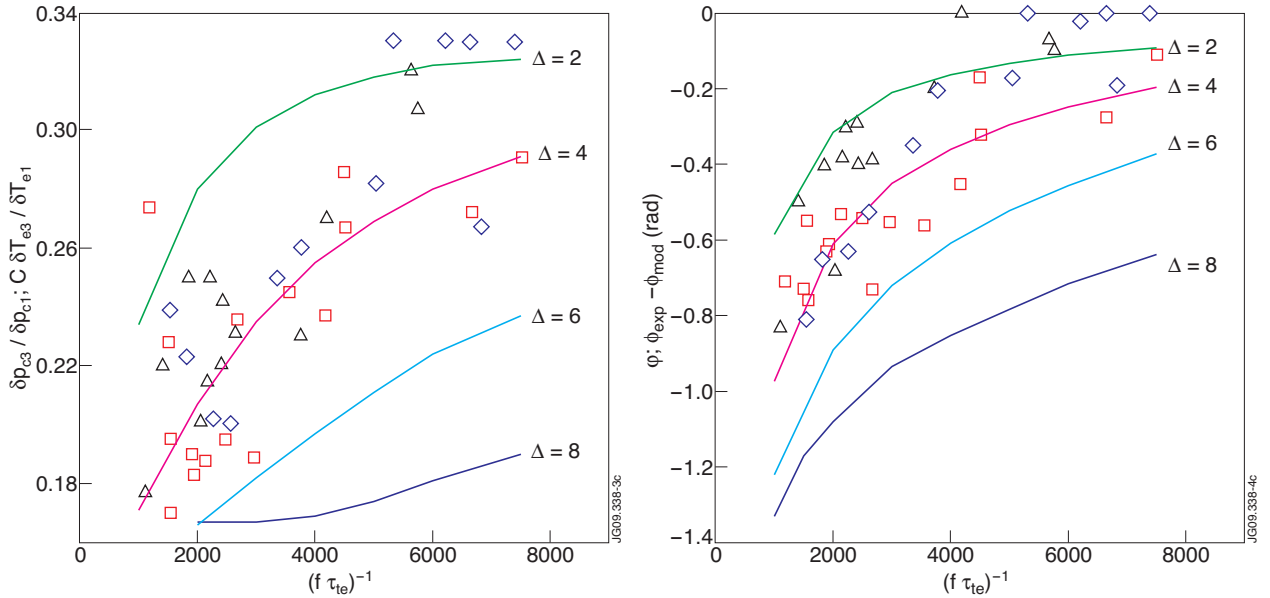

Figure 17: The ratio $\delta p_{C3}/\delta p_{C1}$ (a) as modelled by FP code [38] with $w_1=3.5$, $E/E_{dr}=0$, $T_e=1keV$ and for $\Delta=2$ (green line), 4 (magenta line), 6 (cyan line) and 8 (blue line) and the ratio $C\delta T_{e3}/\delta T_{e1}$ from JET modulated LH experiments at 2.1-2.3T (red squares), 2.7T (black triangles) and 3.4T (blue diamonds) versus normalised period of the modulation, $(ft_{te})^{-1}$. The phase difference $\phi_{exp}-\phi_{mod}$ (b) compared to the phase φ of p_C for $\Delta=2$, 4, 6 and 8.
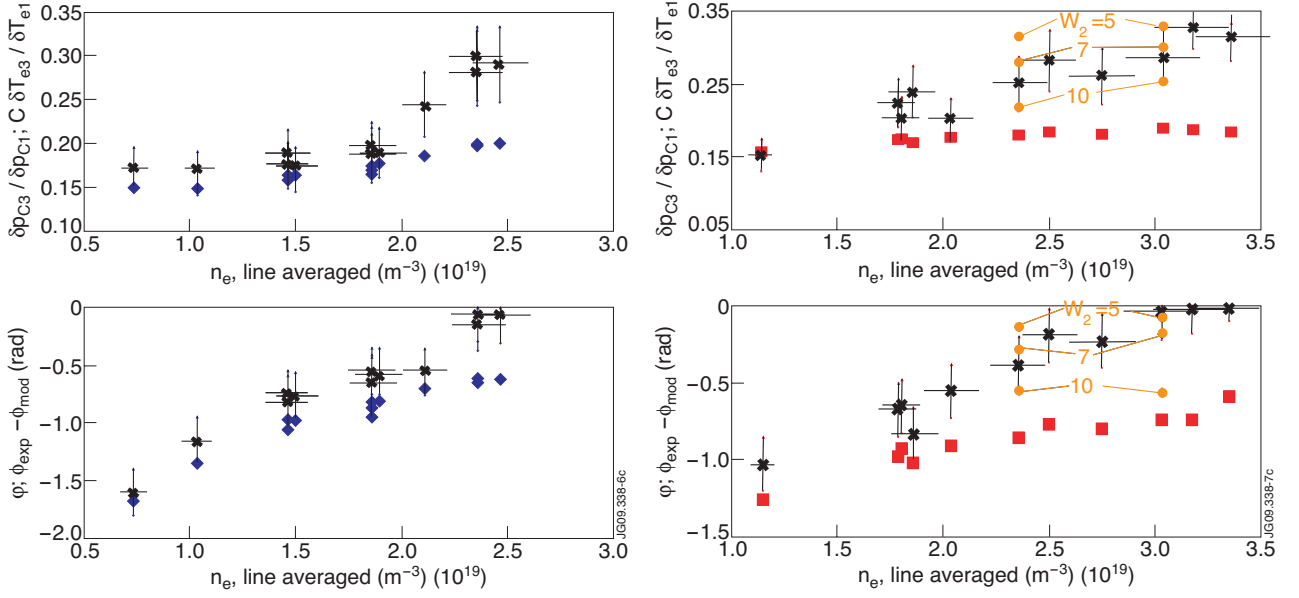
Figure 18: The ratio $C\delta T_{e3}/\delta T_{e1}$ ('x' symbols) compared to $\delta p_{C3}/\delta p_{C1}$ (solid symbols) versus the line averaged density (top graphs) and the phase difference $\phi_{exp}-\phi_{mod}$ compared to j vs. the line averaged density (bottom graphs). The vertical bars indicate the upper and the lower limits of $C\delta T_{e3}/\delta T_{e1}$ and $\phi_{exp}-\phi_{mod}$. Results for 2.1T-2.3T pulses are shown in (a) and 3.4T data are in (b). The solid blue diamond and red square symbols correspond to $\delta p_{C3}/\delta p_{C1}$ and ϕ deduced from FP modelling assuming that $w_1=3$ and $w_2=c/(N_{//acc}v_{te})$. The solid orange circle symbols in (b) are the results for $\delta p_{C3}/\delta p_{C1}$ and ϕ for different values of w_2 as shown in the graph.